1 **Amplified role of potential HONO sources in O_3 formation in North China Plain during**
2 **autumn haze aggravating processes**

3 Jingwei Zhang[1][**], Chaofan Lian[2,3][**], Weigang Wang[2,3][*], Maofa Ge[2,3,6], Yitian Guo[1,3], Haiyan Ran[1,3], Yusheng Zhang[4],
4 Feixue Zheng[4], Xiaolong Fan[4], Chao Yan[5], Kaspar R. Daellenbach[5], Yongchun Liu[4], Markku Kulmala[4,5], Junling
5 An[1,3,6][*]
6 1. State Key Laboratory of Atmospheric Boundary Layer Physics and Atmospheric Chemistry (LAPC), Institute of
7 Atmospheric Physics (IAP), Chinese Academy of Sciences, Beijing 100029, China
8 2. State Key Laboratory for Structural Chemistry of Unstable and Stable Species, Beijing National Laboratory for
9 Molecular Sciences (BNLMS), CAS Research/Education Center for Excellence in Molecular Sciences, Institute of
10 Chemistry, Chinese Academy of Sciences, Beijing 100190, China
11 3. University of the Chinese Academy of Sciences, Beijing 100049, China
12 4. Aerosol and Haze Laboratory, Advanced Innovation Center for Soft Matter Science and Engineering, Beijing
13 University of Chemical Technology, Beijing, 100029, China
14 5. Institute for Atmospheric and Earth System Research/Physics, Faculty of Science, P.O. Box 64, 00014 University
15 of Helsinki, Helsinki, Finland
16 6. Center for Excellence in Urban Atmospheric Environment, Institute of Urban Environment, Chinese Academy of
17 Sciences, Xiamen 361021, China
18 [*]Corresponding author: Weigang Wang (wangwg@iccas.ac.cn), Junling An (anjl@mail.iap.ac.cn)
19 [**]These authors contributed equally.

21 **Abstract:**

22 Co-occurrences of high concentrations of $PM_{2.5}$ and ozone (O_3) have been
23 frequently observed in haze aggravating processes in the North China Plain (NCP) over
24 the past few years, and higher O_3 concentrations during hazy days were supposed to be
25 related to nitrous acid (HONO), but the key sources of HONO enhancing O_3 during
26 haze aggravating processes remain unclear, and will be explored in this study by using
27 the WRF-Chem model, which is improved to include ground-based (traffic, soil, and
28 indoor emissions, and the NO_2 heterogeneous reaction on ground surface (Het_{ground}))
29 and aerosol-related (the NO_2 heterogeneous reaction on aerosol surfaces ($Het_{aerosol}$) and
30 nitrate photolysis ($Phot_{nitrate}$)) potential HONO sources. The results indicate that
31 ground-based HONO sources producing HONO enhancements showed a rapid

decrease with height, while the NO+OH reaction and aerosol-related HONO sources

decreased slowly with height. Phot$_{nitrate}$ contributions to HONO concentrations

enhanced with aggravated pollution levels, the enhanced HONO due to Phot$_{nitrate}$ in

hazy days was about one order of magnitude larger than in clean days and Phot$_{nitrate}$

dominated HONO sources (~30–70% when the ratio of the photolysis frequency of

nitrate (J$_{nitrate}$) to gas nitric acid (J$_{HNO3}$) equals 30) at higher layers (>800 m). Compared

with that in clean days, the Phot$_{nitrate}$ contribution to the enhanced daily maximum 8-h

averaged O$_3$ was increased by over one magnitude during the haze aggravating process.

Phot$_{nitrate}$ contributed only ~5% of the surface HONO in daytime with a J$_{nitrate}$/J$_{HNO3}$

ratio of 30 but contributed ~30–50% of the enhanced O$_3$ near the surface in NCP in

hazy days. Surface O$_3$ was dominated by volatile organic compounds-sensitive

chemistry, while O$_3$ at higher altitude (>800m) was dominated by NO$_x$-sensitive

chemistry. Phot$_{nitrate}$ had a limited impact on nitrate concentrations (<15%) even with a

J$_{nitrate}$/J$_{HNO3}$ ratio of 120. The above results suggest that more field studies of J$_{nitrate}$ in

the atmosphere are still needed.

1. Introduction

Nitrous acid (HONO) is an important source of the hydroxyl radical (OH) through

its photolysis (R1), and contributes ~20–80% of the primary OH production (Alicke et

al., 2002; Hendrick et al., 2014; Kim et al., 2014).

$$HONO + hv \rightarrow NO + OH \quad (R1)$$

53   Although it has passed forty years since the first detection of HONO in the

54   atmosphere (Perner and Platt, 1979), the sources of HONO (especially daytime) and

55   the dynamic parameters of HONO formation mechanisms are still not well understood

56   (Ge et al., 2021), the current air quality models with the default gas-phase reaction (the

57   reverse reaction of R1) always severely underestimate HONO observations, resulting

58   in low atmospheric oxidation capacity and underestimation of secondary pollutants like

59   ozone (O_3) (Li et al., 2010, 2011; Sarwar et al., 2008; Zhang et al., 2016, 2019a).

60   HONO sources can be generally classified into three categories, i.e., direct

61   emissions, homogeneous and heterogeneous reactions. Direction emissions are mainly

62   from traffic (Kramer et al., 2020; Kurtenbach et al., 2001; Liao et al., 2021), soil

63   (Kubota and Asami, 1985; Oswald et al., 2013; Wu et al., 2019; Xue et al., 2021),

64   biomass burning (Cui et al., 2021; Rondon and Sanhueza, 1989; Theys et al., 2020) and

65   indoor combustion processes (Klosterkother et al., 2021; Liu et al., 2019; Pitts et al.,

66   1985). The reaction of nitric oxide (NO) with OH is usually thought as the dominant

67   homogeneous reaction and is important during daytime but could be neglected at night

68   due to low OH concentrations. The heterogeneous reactions mainly include nitrogen

69   dioxide (NO_2) hydrolysis and reduction reactions on various humid surfaces

70   (Finlayson-Pitts et al., 2003; Ge et al., 2019; Gómez Alvarez et al., 2014; Ma et al.,

71   2013; Marion et al., 2021; Sakamaki et al., 1983; Tang et al., 2017; Yang et al., 2021b)

72   and nitrate photolysis (Romer et al., 2018; Zhou et al., 2003), and are usually thought

73   as the main contributor to HONO concentrations in the atmosphere.

74   Among those potential HONO sources, the photolysis of nitrate to produce HONO

75 in the atmosphere has received extensive attention over the past several years, and the

76 nitrate photolysis frequency ($J_{nitrate}$) is still argued. In the laboratory studies, some

77 researchers (Bao et al., 2018; Ye et al., 2016, 2017) showed that nitrate photolysis was

78 an important HONO source, the measured $J_{nitrate}$ was 1–3 orders larger than the gaseous

79 nitric acid (HNO_3) photolysis frequency (J_{HNO3}) and could reach up to 10^{-4} s^{-1}, and a

80 number of substances including humic acid (Yang et al., 2018), sulfate (Bao et al., 2020)

81 and TiO_2 (Xu et al., 2021) might enhance the reaction significantly; while Shi et al.

82 (2021) found that the $J_{nitrate}/J_{HNO3}$ ratio was <10 when using suspended submicron

83 particulate sodium and ammonium nitrate rather than $PM_{2.5}$ samples. In the field studies

84 combining with model simulations, Kasibhatla et al. (2018) compared NO_x

85 observations in Cape Verde Atmospheric Observatory with GEOS-Chem (Goddard

86 Earth Observing System-Chemistry) model simulations and reported a $J_{nitrate}/J_{HNO3}$ ratio

87 of 25–50, Romer et al. (2018) reported a $J_{nitrate}/J_{HNO3}$ ratio of < 30 based on observations

88 of NO_x (= NO + NO_2) and HNO_3 over the Yellow Sea and a box model simulation.

89 Adopting a $J_{nitrate}/J_{HNO3}$ ratio of ~120 could greatly improve daytime surface HONO

90 simulations (contributed ~30–40% of noontime HONO) by using the Community

91 Multiscale Air Quality model (CMAQ) in the Pearl River Delta (Fu et al., 2019) or a

92 box model in the Yangtze River Delta (Shi et al., 2020), while a $J_{nitrate}/J_{HNO3}$ ratio of 30

93 produced negligible HONO in clean periods (~2%) and slightly higher HONO in heavy

94 haze periods (~8%) in the North China Plain (NCP) by using a box model (Xue et al.,

95 2020) and ~1% by using CMAQ model in urban Beijing (Zhang et al., 2021). Recently,

96 Zheng et al. (2020) evaluated the effect of three $J_{nitrate}/J_{HNO3}$ ratios (1, 10 and 100) on

97 heterogeneous sulfate formation by using CMAQ and large uncertainties of simulated

98 sulfate concentrations were reported, so more efforts are needed to better understand

99 the impact of nitrate photolysis on HONO concentrations, atmospheric oxidation

100 capacity and other secondary pollutant concentrations.

101   A number of potential HONO sources (e.g., direct emissions, NO_2 heterogeneous

102 reactions and nitrate photolysis) have been coupled into several air quality models (An

103 et al., 2013; Fu et al., 2019; Guo et al., 2020; Li et al., 2010, 2011; Sarwar et al., 2008;

104 Tang et al., 2015; Xu et al., 2006; Zhang et al., 2019a, 2019b, 2020a, 2021, 2022) to

105 improve HONO simulations. The improved HONO sources can produce more OH,

106 which is favorable for the formation of O_3 (Fu et al., 2019; Guo et al., 2020; Li et al.,

107 2010; Xing et al., 2019; Zhang et al., 2016, 2019a, 2022). O_3 can directly damage plants

108 and threaten human health (Avnery et al., 2011a, b; Feng et al., 2015, 2019; Mills et al.,

109 2007, 2018; Richards et al., 1958; Selin et al., 2009; Wilkinson et al., 2012), an

110 increasing trend of O_3 concentrations in China has been widely reported in recent years

111 (Chen et al., 2020a; Li et al., 2020; Lu et al., 2020; Ma et al., 2016; Maji and Namdeo,

112 2021), made O_3 pollution be a severe concern. A co-occurrence of high $PM_{2.5}$ and O_3

113 concentrations has been frequently found in China over the past few years and

114 researchers speculated the significant role of HONO in producing O_3 enhancements

115 (Feng et al., 2021; Fu et al., 2019; Tie et al., 2019; Yang et al., 2021a), but the HONO

116 difference in O_3 formation during clean and hazy days is still unclear, and the relative

117 contribution of each potential HONO source to O_3 enhancements during haze

118 aggravating processes with a co-occurrence of high $PM_{2.5}$ and O_3 concentrations is still

119   unknown to the best of our knowledge.

120   In this study, time series of pollutants including HONO, O_3, and nitrate were

121   collected in NCP in Oct.11–31 of 2018, in which high concentrations of $PM_{2.5}$

122   accompanying by high O_3 concentrations were found at least twice in haze events, thus

123   the specific role of each of potential HONO sources coupled into the Weather Research

124   and Forecasting model with Chemistry (WRF-Chem) in O_3 formation will be explored

125   during these haze events. The relative contribution of each potential HONO source to

126   surface-averaged and vertical-averaged concentrations of HONO and O_3 will be

127   quantified and the uncertainty in key potential HONO sources (e.g., $J_{nitrate}$) will be

128   discussed, in order to find the key HONO sources resulting in O_3 enhancements in NCP

129   in different pollution levels (especially during haze aggravating processes).

130   **2. Data and methods**

131   **2.1 Observed data**

132   The field observation was carried out during October 11–31, 2018, and the

133   observation site was located in the west campus of Beijing University of Chemical

134   Technology (BUCT, 116°18'37'' E, 39°56'56'' N) in Beijing. BUCT is an urban site

135   close to the third ring road of Beijing, with large human activities, including vehicle

136   emissions. Instruments were set on the 5th floor of the main teaching building. HONO

137   was measured with a home-made water-based long-path absorption photometer (Chen

138   et al., 2020b). A set of on-line commercial analyzers (Thermo 48i, 42i, 49i, 43i) was

139   used for measurements of CO, NO_x, O_3, and SO_2. The chemical composition of $PM_{2.5}$

140   was analyzed with a Time-of-Flight Aerosol Chemical Speciation Monitor (ToF-ACSM,

141   Aerodyne). An online Single Photon Ionization Time-of-Flight Mass Spectrometer

142   (SPI-ToF-MS, Hexin) was used for the detection of a large variety of volatile organic

143   compounds (VOCs) (Gao et al., 2013). Surface observations of O_3, NO_2, $PM_{2.5}$ and

144   PM_{10} at 95 sites in NCP were obtained from https://quotsoft.net/air/, issued by the China

145   Ministry of Ecology and Environment; surface meteorological observations at 284 sites

146   in NCP were taken from the National Climatic Data Center, China Meteorological

147   Administration (**Fig.1**).

148   The vertical HONO observations was not available during the Oct.11–31 of 2018

149   at the BUCT site, we used the observed vertical HONO concentrations from Meng et

150   al. (2020) at urban Beijing in December of 2016 to validate our simulation of vertical

151   HONO concentrations, which were also used by Zhang et al. (2021) in their CMAQ

152   model validation.

153

154   **2.2 Model description**

155   The improved WRF-Chem (version 3.7.1), which contained six potential HONO

156   sources, i.e., traffic ($E_{traffic}$), soil (E_{soil}), and indoor (E_{indoor}) emissions, nitrate photolysis

157   in the atmosphere ($Phot_{nitrate}$), and NO_2 heterogeneous reactions on aerosol ($Het_{aerosol}$)

158   and ground (Het_{ground}) surfaces (Zhang et al., 2019a), was used in this study. $Phot_{nitrate}$

159   was newly added in WRF-Chem (R2) following the work of Fu et al. (2019), Ye et al.

160   (2017), and Zhou et al. (2003):

161    $$pNO_3 + hv \rightarrow 0.67HONO + 0.33NO_2 \quad \text{(R2)}$$
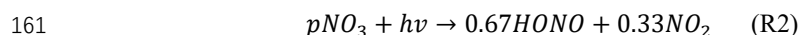
162   The uptake coefficient (γ) of NO_2 on aerosol surfaces, and the yield (f) of HONO from

163   NO_2 reaching the ground surface were improved from previous studies (Li et al., 2010;

164   Liu et al., 2014; Zhang et al., 2019a) and calculated by:

165    $$\gamma = 5 \times 10^{-6} \times \left(1 + \frac{SR}{\alpha}\right) \quad (R3)$$

166    $$f = 0.08 \times \left(1 + \frac{SR}{\alpha}\right) \quad (R4)$$

167   where SR denotes solar radiation (W m^{-2}), α is an adjusted parameter and set as 100,

168   thus γ and f became continuous functions during the whole day (γ and f enhanced by

169   one order of magnitude and reached 5×10^{-5} and 0.8 when SR reached 900 W m^{-2} at

170   noontime, respectively).

171   The physical and chemical schemes used in this study are given in **Table 1**. Two

172   domains were adopted, domain one contains 82×64 grid cells with a horizontal

173   resolution of 81 km, domain two contains 51×51 grid cells with a horizontal resolution

174   of 27 km (**Fig.1**), both with 17 vertical layers encompassing from the surface to 100

175   hPa. The observational sites are shown in the right panel of **Fig.1**, including one HONO

176   observation site (the orange dot in urban Beijing), 95 observation sites of $PM_{2.5}$, NO_2

177   and O_3 (pink dots) and 284 meteorological monitoring sites (black dots).
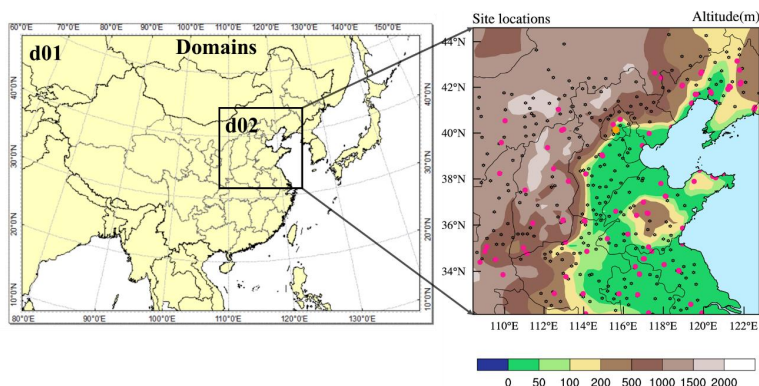
178

179   **Figure 1** Domains of WRF-Chem used in this study (left panel), and the locations of one HONO

180   observation site (the orange dot in urban Beijing), 95 environmental monitoring ($PM_{2.5}$, NO_2 and

181   O_3) sites (deep pink dots), and 284 meteorological observation sites (black dots) in domain 2 (right

182   panel).

183

184   The anthropogenic emissions in East Asia in 2010 were taken from the MIX emission

185   inventory (Li et al., 2017) (http://www.meicmodel.org/), including both gaseous and

186   aerosol species, i.e., SO_2, NO_x, CO, VOCs, NH_3, PM_{10}, $PM_{2.5}$, BC, OC and CO_2, and

187   were provided monthly by five sectors (power, industry, residential, transportation, and

188   agriculture) at a resolution of $0.25° \times 0.25°$. VOC emissions were speciated into model-

189   ready inputs according to the MOZART chemical mechanism to build the WRF-Chem

190   emission files. The anthropogenic emissions in China were replaced by employing the

191   MEIC 2016 (the Multi-resolution Emission Inventory for China) developed by

192   Tsinghua University. The NH_3 emissions in China were from Dong et al. (2010),

193   biomass burning emissions were from Huang et al. (2012) and biogenic emissions were

194   calculated using the Model of Emissions of Gases and Aerosols from Nature (MEGAN)

195   (Guenther et al., 2012). Due to the sharp reduction of anthropogenic emissions in recent

196   years, the default emission inventory was systematically overestimated in autumn of

197   2018, especially for SO_2 and $PM_{2.5}$ concentrations. Based on the comparison of

198   simulations and observations (the urban Beijing site plus other 95 pollutant monitoring

199   sites in NCP), we cut off 80% of SO_2 emissions, 50% of NH_3 emissions, 30% of toluene

200   emissions, and 50% of $PM_{2.5}$ and PM_{10} emissions. The cut-off emissions are largely

201   close to the emission reductions in east China during 2013 to 2017 (Zhang and Geng,

202   2019). The revised emissions significantly improved regional $PM_{2.5}$ simulations in NCP

203   **(Fig.S1)**, and the simulations of gases and $PM_{2.5}$ in urban Beijing **(Fig.S2)**.

204   The National Centers for Environmental Prediction (NCEP) $1° \times 1°$ final reanalysis

205   data (FNL) (https://rda.ucar.edu/datasets/ds083.2/) were used in this study to obtain the

206   meteorological initial and boundary conditions every 6 h. The global simulations of

207   MOZART-4 (https://www.acom.ucar.edu/wrf-chem/mozart.shtml) were used as the

208   chemical initial and boundary conditions (every 6 h).

209

210   **Table1** Physical and chemical options in WRF-Chem used in this study

Options	WRF-Chem
Advection scheme	Runge-Kutta 3rd order
Boundary layer scheme	YSU
Cloud microphysics	Lin et al. (1983)
Cumulus parameterization	New Grell scheme
Land-surface model	Noah
Long-wave radiation	RRTM
Short-wave radiation	Goddard
Surface layer	Revised MM5 Monin-Obukhov scheme
Aerosol option	MOSAIC
Chemistry option	Updated MOZART mechanism
Photolysis scheme	F-TUV

211

212   Totally 23 simulation scenarios were performed in this study (**Table 2**), in which

213   the base case only considered the default homogeneous reaction (OH + NO → HONO),

214   case 6S contained six potential HONO sources while case A, B, C, D, E and F contained

215   each of the six potential HONO sources, respectively. Other 15 cases (A_double,

216   A_half, …, Nit_120, D_NO₂ and D_HONO) were used to evaluate the uncertainties of

217   the six potential HONO sources (**Table 2**). All of the cases were simulated with a spin-

218   up of 7 days. $J_{nitrate}$ and J_{HNO3} denote the photolysis frequency of nitrate and gas nitric

219   acid in the atmosphere, respectively; the enhancement factor for F_double was 1.25

220   rather than 2.0 to avoid the production rate of HONO from NO_2 reaching the surface

221   exceeding 100%, while $0.33NO_2$ in D_NO_2 or 0.67HONO in D_HONO referred to the

222   assumed products of the nitrate photolysis in R2.

223

224   **Table 2.** Simulation scenarios designed in this study.

Case	HONO sources
Base	Default (OH + NO $\rightarrow$ HONO)
6S	Default + $E_{traffic}$ + E_{soil} + E_{indoor} + $Phot_{nitrate}$ ($J_{nitrate}/J_{HNO3}$ = 30) + $Het_{aerosol}$ + Het_{ground}
A	Default + $E_{traffic}$
B	Default + E_{soil}
C	Default + E_{indoor}
D	Default + $Phot_{nitrate}$ ($J_{nitrate}/J_{HNO3}$ = 30)
E	Default + $Het_{aerosol}$
F	Default + Het_{ground}
A_double	Default + $2 \times E_{traffic}$
A_half	Default + $0.5 \times E_{traffic}$
B_double	Default + $2 \times E_{soil}$
B_half	Default + $0.5 \times E_{soil}$
C_double	Default + $2 \times E_{indoor}$
C_half	Default + $0.5 \times E_{indoor}$
E_double	Default + $Het_{aerosol}$ ($2 \times \gamma$)
E_half	Default + $Het_{aerosol}$ ($0.5 \times \gamma$)
F_double	Default + Het_{ground} ($1.25 \times f$)
F_half	Default + Het_{ground} ($0.5 \times f$)
Nit_1	Default + $Phot_{nitrate}$ ($J_{nitrate}/J_{HNO3}$ =1)
Nit_7	Default + $Phot_{nitrate}$ ($J_{nitrate}/J_{HNO3}$ = 7)
Nit_120	Default + $Phot_{nitrate}$ ($J_{nitrate}/J_{HNO3}$ = 120)
D_NO_2	Only $0.33NO_2$ produced in $Phot_{nitrate}$ for case D
D_HONO	Only 0.67HONO produced in $Phot_{nitrate}$ for case D

225   **3.Results**

226   **3.1 Comparison of simulations and observations**

227   **3.1.1 Meteorological factors**

228   The statistical metrics of simulated meteorological parameters at 284 sites in NCP

229   including air temperature (T), relative humidity (RH) and wind speed (WS) were

230   comparable with the previous modelling results of other researchers (**Table 3**), the

231   simulated wind direction (WD) bias within 45° accounted for ~56%, and the bias within

232   90° accounted for ~80%, suggesting that the simulated WD captured the main observed

233   WD.

234

235   **Table 3.** Performance metrics (index of agreement (IOA), RMSE (root-mean-square error) and

236   MB (mean bias)) of WRF-Chem simulated air temperature, relative humidity, wind speed and

237   direction at 284 meteorological sites in the North China Plain during Oct. 11–31 of 2018. The

238   definition of the metrics used in this study is given in **Text S1**.

	IOA	RMSE	MB	Reference
T (℃)	**0.97**	**1.4**	**-1.1**	**This work**
	0.90	2.5	0.2	(Wang et al., 2014)
	0.90	/	-0.9	(Wang et al., 2010)
	0.88	/	0.5	(Li et al., 2012)
	/	3.1	0.8	(Zhang et al., 2012)
RH (%)	**0.90**	**9.0**	**-7.1**	**This work**
	0.78	16.3	-5.5	(Wang et al., 2014)
	0.78	/	-1.3	(Wang et al., 2010)
	0.86	/	-1.1	(Li et al., 2012)
	/	17.4	-5.7	(Zhang et al., 2012)
WS (m s^{-1})	**0.48**	**1.4**	**1.3**	**This work**
	0.56	2.5	1.6	(Wang et al., 2014)
	0.65	2.1	0.9	(Wang et al., 2010)
	0.62	1.5	0.6	(Li et al., 2012)
	/	2.2	1.1	(Zhang et al., 2012)
WD Bias	*0-45°*	*45-90°*	*>90°*	
Count	*75701*	*21500*	*28075*	*135276(Total)*
Percentage	**55.96%**	**23.29%**	**20.75%**	

239   **3.1.2 Pollutant concentrations at the BUCT site**

240   Time series of the observational data at the BUCT site are shown in **Fig.2**, the gray

241   shaded periods stand for three haze aggravating processes, while the cyan shaded period

242   denotes typical clean days, respectively. The hourly largest observations of O$_3$ (~50–75

243   ppb) and PM$_{2.5}$ (~100–200 µg/m^3) were both relatively higher in hazy days than in clean

244   days, especially for the first two haze events (the O$_3$ concentrations in the third haze

245   event was relatively lower due to the higher NO$_x$ concentrations in urban area).

246   The observed PM$_{2.5}$ and nitrate trends at the BUCT site were well simulated

247   **(Fig.2a&b)**, and NO$_2$ simulations generally agreed with the observations **(Fig.2c)**.

248   Hourly and diurnal HONO simulations at the BUCT site **(Fig.2d&3a)** were

249   significantly improved in the 6S case (mean is 1.47 ppb) compared with the base case

250   (mean is 0.05 ppb). The normalized mean bias (NMB) was remarkably reduced to -

251   14.22% (6S) from -97.11% (Base), and the index of agreement (IOA) was improved

252   significantly to 0.86 (6S) from 0.78 (Base) **(Fig.2d)**.

253   As for O$_3$, noticeable improvements could be found at the BUCT site after

254   considering the six potential HONO sources, especially in hazy days **(Fig.2e&f)**. The

255   mean bias (MB) was improved to -3.61 ppb (6S) from -7.09 ppb (Base), and the IOA

256   was improved to 0.80 (6S) from 0.45 (Base) **(Fig.2e)**. Specially, the 6S case

257   significantly enhanced daytime hourly O$_3$ by 15–35 ppb compared with the base case

258   and the simulated O$_3$ was very close to the observations in hazy days **(Fig.2e)**. Larger

259   daytime O$_3$ enhancements were accompanied with higher PM$_{2.5}$ concentrations during

260   haze aggravating processes, while in clean days the daytime enhanced O$_3$ due to the

261   potential HONO sources was mostly < 5 ppb **(Fig.2e&f)**. The diurnal O$_3$ pattern during

262   the first two haze aggravating processes is presented in **Fig.3b**, significant

263   improvements in daily maximum 8-h (10:00–17:59) averaged (DMA8) O$_3$ (18.8 ppb)

264   occurred at the BUCT site after considering the six potential HONO sources, and the

265   NMB of DMA8 O_3 was remarkably improved to -2.38% (6S) from -47.14% (Base).

266
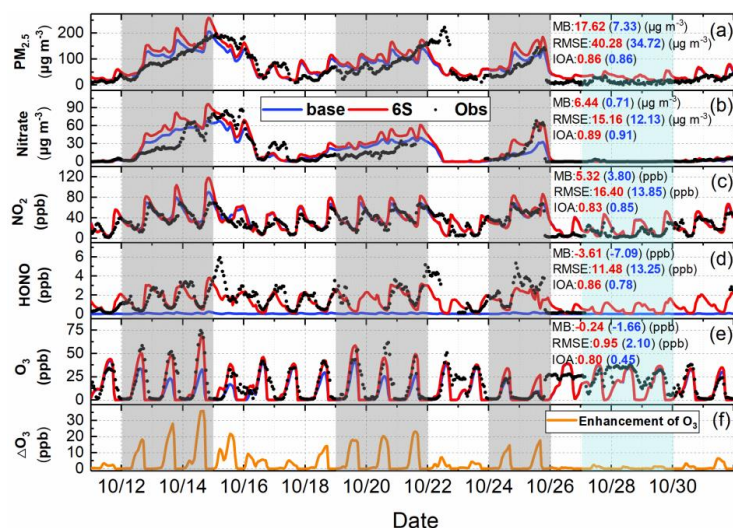
267

268   **Figure 2** Comparison of simulated (Base and 6S cases) and observed hourly concentrations of $PM_{2.5}$,

269   nitrate, NO_2, HONO and O_3 (a–e), and the hourly enhanced concentrations of O_3 ($\triangle O_3$) (f) caused

270   by the six potential HONO sources (6S minus Base) at the BUCT site during Oct.11–31 of 2018.

271

272
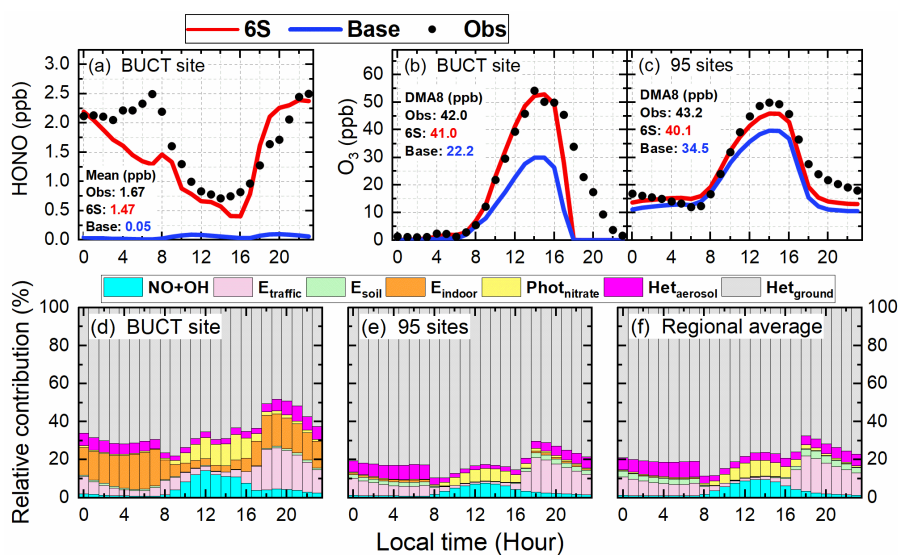
Figure 3 Comparison of diurnal mean simulations (Base and 6S cases) and observations of HONO

during the study period (a) and O_3 during the first two haze events at the BUCT site (b), and O_3

averages at the 95 NCP monitoring sites during the study period (c); and the relative contributions

of each of the six potential HONO sources and the reaction of OH with NO to surface HONO

concentrations for the 6S case at the BUCT site (d), at the 95 monitoring sites (e) and in the whole

NCP region (f). The calculated 24-h mean HONO concentrations and DMA8 O_3 concentrations

were given in panels (a) – (c).

The relative contribution of each HONO source near the surface at the BUCT site

for the 6S case is shown in **Fig.3d.** Briefly, Het_{ground} was the largest source during

daytime and nighttime (~50–70%), consistent with the results of Zhang et al. (2021).

$Phot_{nitrate}$ ($J_{nitrate}/J_{HNO3}$ = 30) and the NO+OH reaction contributed similarly ~1–12%

during daytime. $E_{traffic}$ was important during nighttime (~10–20%) but small during

daytime (<5%). The contribution of $Het_{aerosol}$ to HONO concentrations was minor (~2–

288   3%) in daytime and ~6–10% in nighttime. E_{soil} could be neglected while the

289   contribution of E_{indoor} was close to that of $E_{traffic}$ in urban Beijing. The relative

290   contribution of the potential HONO sources in this study was comparable with the result

291   of Fu et al. (2019) by using CMAQ, except for the contribution of $Phot_{nitrate}$ due to the

292   different $J_{nitrate}/J_{HNO3}$ ratios (30 in our study and ~120 in Fu et al. (2019)).

293

294   **3.1.3 Pollutant concentrations in NCP**

295   The 95-site-averaged hourly simulations and observations of O_3, NO_2 and $PM_{2.5}$

296   during the study period are shown in **Fig.4**. The six potential HONO sources

297   significantly improved hourly O_3 simulations, remarkably enhanced the daily

298   maximum O_3 by ~5–10 ppb during Oct. 11–25, and by ~2–4 ppb during Oct. 26–31

299   (**Fig.4a&b**). The simulations of NO_2 well agreed with the observations, and the mean

300   concentrations were 22.55 (Base), 21.62 (6S) and 20.74 (Obs) ppb (**Fig.4c**). The $PM_{2.5}$

301   simulations generally followed the observed $PM_{2.5}$ trend but were overestimated by ~8

302    $\mu g\ m^{-3}$, with averaged concentrations of 49.94 (Base), 53.30 (6S) and 45.31 (Obs) μg

303   m^{-3} (**Fig.4d**), respectively.

304

305
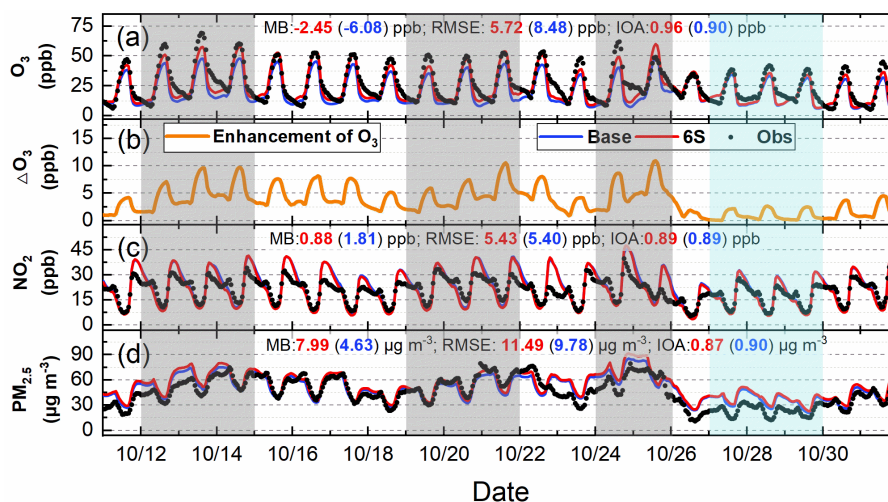
Figure 4 Comparison of 95-site-mean simulated (Base and 6S cases) and observed hourly O_3(a), NO_2 (c)

and $PM_{2.5}$ (d), and O_3 enhancements due to the six potential HONO sources (6S minus Base case) (b) in

the North China Plain during Oct.11–31 of 2018.

309

310   The 95-site-averaged diurnal simulations and observations of O_3 are presented in

311   **Fig.3c**, O_3 simulations showed a remarkable improvement when the six potential

312   HONO sources were considered, the six potential HONO sources produced a mean

313   enhancement of 5.7 ppb in DMA8 (10:00–17:59) O_3 and improved the NMB from -

314   20.32% to -7.16% at the 95 sites in NCP. The 95-site-averaged diurnal simulations and

315   observations of NO_2 and $PM_{2.5}$ during the study period are demonstrated in **Fig. S3**.

316   NO_2 simulations generally followed the observed trend but were underestimated during

317   04:00 to 16:00 and overestimated after 18:00 (**Fig.S3a**), $PM_{2.5}$ simulations agreed with

318   the observed diurnal pattern but were overestimated for both cases during the whole

319   day (**Fig.S3b**).

320   The relative contribution of each HONO source near the surface at the 95 NCP sites

321   for the 6S case is shown in **Fig.3e.** Het$_{ground}$ was the dominant source during daytime

322   and nighttime (~70–80%). Phot$_{nitrate}$ (J$_{nitrate}$/J$_{HNO3}$ = 30) and the NO+OH reaction nearly

323   equaled and contributed ~2–8% during daytime (~5% on average). E$_{traffic}$ was important

324   during nighttime (~10–15%) but small during daytime (<3%). The contribution of

325   Het$_{aerosol}$ to HONO concentrations was <3% in daytime and <10% in nighttime. E$_{soil}$

326   contributed ~3% in nighttime but could be neglected in daytime. The contribution of

327   E$_{indoor}$ was too small to be noticed at the 95 NCP sites, implying that this source was

328   noticeable only in megacities. The relative contribution of each HONO source in the

329   whole NCP region (all grid cells in domain two except for the seas) is presented in

330   **Fig.3f**, the results were quite similar with those at the 95 sites (**Fig.3f**), thus the results

331   of the 95 sites were representative for the whole NCP region. To further understand the

332   role of potential HONO sources in haze aggravating processes in regional O$_3$

333   concentrations, the 95 site-averaged surface/vertical HONO concentrations and their

334   impacts during a typical haze event (Oct. 19–21) and a clean period (Oct. 27–29) were

335   analyzed and shown in the following sections.

336

3.2 Spatial distribution of enhanced DMA8 O$_3$ by potential HONO sources

3.2.1 General patterns of enhanced DMA8 O$_3$

339   **Fig.S4** shows surface-averaged and zonally-averaged DMA8 O$_3$ enhancements due

340   to the six potential HONO sources in NCP during the study period (Oct.11-31) and three

341   haze events (Oct.12–14, Oct.18–21 and Oct.24–25). The overall surface DMA8 O$_3$

342   enhancement decreased gradually from south (6–10 ppb) to north (2–6 ppb) (**Fig.S4a**)

343   and could reach 10–20 ppb under unfavorable meteorological conditions during haze

344   events (**Fig.S4b–d**). For the first two haze events, the anti-cyclone in the Shandong

345   peninsula carried pollutants being transported from the southeastern NCP to the western

346   (108–112°E) and northern (39–41°N) NCP, and the six potential HONO sources led to

347   a DMA8 O_3 enhancement of 10–20 ppb (**Fig.S4b**) and 10–15 ppb (**Fig.S4c**) in Beijing,

348   respectively. For the third haze event, two air masses were converged to form a transport

349   channel from south to north, the O_3 enhancement caused by the six potential HONO

350   sources can reach 10–18 ppb in the southern NCP and decreased to 6–10 ppb in the

351   northern NCP along the transport channel. Vertically, the DMA8 O_3 enhancements were

352   2–8 ppb during the whole period (**Fig.S4e**) and increased to 6–12 ppb in these haze

353   events (**Fig.S4f–h**). The enhanced O_3 near the surface (0–100 m) was slightly smaller

354   than that at higher altitude (**Fig.S4f–h**), due mainly to the stronger titration of O_3 by

355   NO near the surface. The above results demonstrated that the six potential HONO

356   sources significantly enhanced surface and vertical O_3 concentrations in NCP,

357   especially during haze events.

358

359   3.2.2 During a typical haze aggravating process and a clean period

360   **Fig.5** demonstrates surface-averaged and zonally-averaged DMA8 O_3

361   enhancements due to the six potential HONO sources in NCP during a typical haze

362   aggravating process (Oct.19–21, 2018) and a clean period (Oct.27–29, 2018). The

363   increasing trend of DMA8 O₃ enhancements can be clearly seen from Oct.19 to Oct.21

364   near the surface and in the vertical direction. During the haze aggravating process, the

365   surface DMA8 O₃ enhancements were ~2–10 ppb (Oct.19), ~6–12 ppb (Oct.20) and

366   ~8–15 ppb (Oct.21), respectively, and the vertical DMA8 O₃ enhancements were ~4–7

367   ppb (Oct.19), ~6–10 ppb (Oct.20), and ~8–15 ppb (Oct.21), respectively; while during

368   clean days, the surface/vertical DMA8 O₃ enhancements were usually <4 ppb. The six

369   potential HONO sources significantly enhanced surface and vertical O₃ concentrations

370   in NCP during haze aggravating processes, the detailed role of potential HONO sources

371   on vertical HONO concentrations and their impacts were given in the next section.

372

373

374

375

376
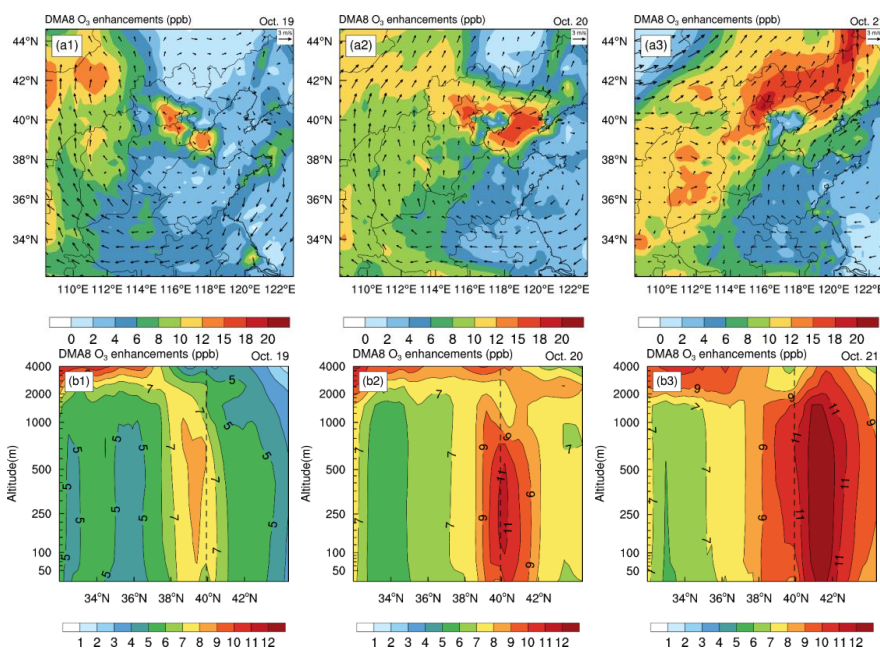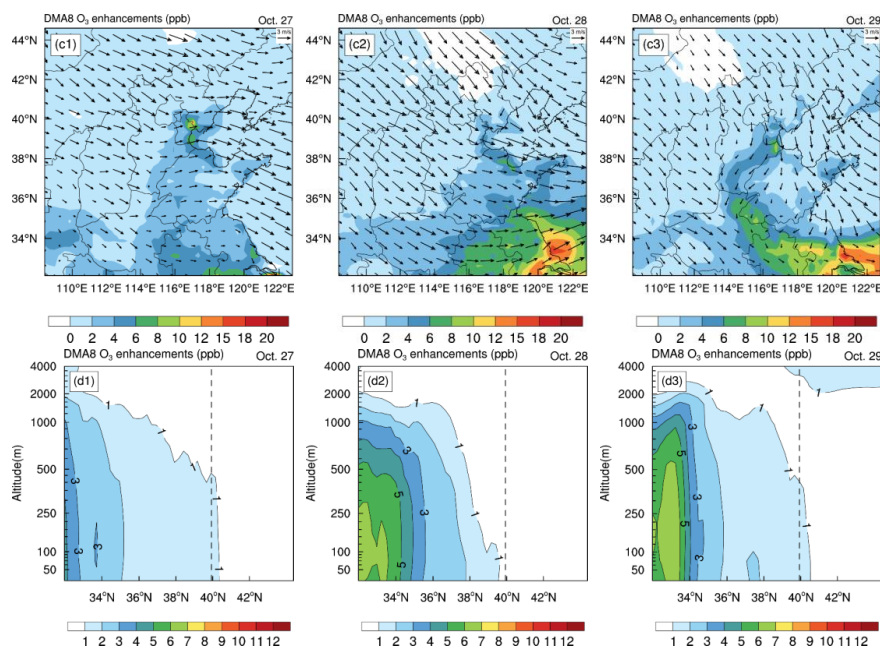
Figure 5 Surface-averaged (a1–a3, c1–c3) and zonally-averaged (b1–b3, d1–d3) DMA8 O_3

enhancements due to the six potential HONO sources in the North China Plain during a typical haze

aggravating process (Oct.19–21, 2018) and a clean period (Oct.27–29, 2018). The dashed line

denotes the latitude of the BUCT site.

381

3.3 Vertical variations of potential HONO sources and their impacts

3.3.1 Potential HONO sources and their impacts on HONO concentrations

A number of studies have conducted vertical HONO observations abroad

(Kleffmann et al., 2003; Ryan et al., 2018; Sorgel et al., 2011; VandenBoer et al., 2013;

Villena et al., 2011; Wang et al., 2020; Wong et al., 2011, 2012; Zhang et al., 2009) and

in China (Meng et al., 2020; Wang et al., 2019; Xing et al., 2021; Zhu et al., 2011), a

388   decreasing trend of HONO with height was mostly observed among these studies, and

389   our simulations also reproduced this vertical variation and were comparable with

390   another model simulation by Zhang et al. (2021) whom using the CMAQ model

391   (**Fig.S5**). For a deep understanding of the role of each considered HONO source in

392   HONO concentrations at different heights, we assessed the contributions of each

393   potential HONO source to HONO concentrations at different heights (**Fig.6**) during

394   Oct.11–31 of 2018.

395   Generally, the impacts of ground-based potential HONO sources ($E_{traffic}$, E_{soil},

396   E_{indoor} and Het_{ground}) on HONO concentrations decreased rapidly with height, while the

397   NO+OH reaction and aerosol related HONO sources ($Phot_{nitrate}$ and $Het_{aerosol}$) decreased

398   slowly with height (**Fig.6**). During daytime the NO+OH reaction, $Phot_{nitrate}$ and Het_{ground}

399   were the three main HONO sources, while during nighttime $E_{traffic}$, $Het_{aerosol}$ and

400   Het_{ground} were the three main contributors to HONO concentrations (**Fig.6**). The HONO

401   concentrations via the NO+OH reaction and $Phot_{nitrate}$ were higher during daytime. The

402   impact of E_{soil} in the NCP was small, however, Xue et al. (2021) found strong HONO

403   emissions in NCP agricultural fields after fertilization, suggesting that this source may

404   have a remarkable enhancement on regional HONO and secondary pollutants in crop

405   growing seasons.

406
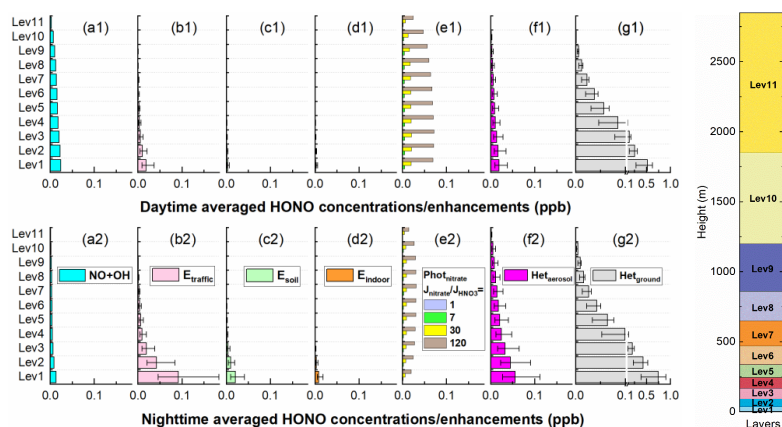
Figure 6 The 95-site-averaged daytime/nighttime HONO concentrations/enhancements at different

heights when the NO+OH reaction (a1&a2) and each of the six potential HONO sources (b1–

g1&b2–g2) were considered during Oct.11–31 of 2018, the error bar denotes the uncertainties of

each potential HONO source in HONO concentrations (**Table 2**). The right panel denotes the

approximate height of each vertical layer above the ground.

The comparison of HONO concentrations/enhancements during a haze aggravating

process and a clean period is shown in **Fig.7&8**. Generally, daytime HONO

concentrations increased in haze aggravating processes and were higher than those in

clean days. Het$_{ground}$ was the dominant source of the surface HONO in both hazy and

clean days and contributed 80–90% of daytime averaged HONO concentrations (**Fig.8**),

however, its relative contribution decreased with height, especially in haze aggravating

processes (**Fig.8**). Although the contribution of the NO+OH reaction to daytime HONO

was small near the surface, its relative contribution to HONO increased with height,

especially in clean days (**Fig.8**). As for Phot$_{nitrate}$, a much larger enhancement could be

found in hazy days compared with clean days. In clean days the daytime enhanced

424   HONO by Phot$_{nitrate}$ was only 1–3 ppt in general and its contribution to daytime HONO

425   was usually <10%, while in the haze aggravating process, the enhanced HONO

426   concentration by Phot$_{nitrate}$ was about one order of magnitude higher than that in clean

427   days and Phot$_{nitrate}$ became the dominant HONO source (~30–70%) at higher altitude,

428   and both HONO concentrations and Phot$_{nitrate}$ contributions increased with the air

429   pollution aggravation (**Fig.7a–c, Fig.8a–c**). The contributions of direct emission

430   sources were small and decreased when PM$_{2.5}$ increased, compared with those

431   heterogeneous reactions. Higher concentrations of NO$_2$, nitrate, and PM$_{2.5}$ favored

432   heterogeneous formation of HONO, while direct emission sources were relatively

433   invariable under different pollution levels.

434   Based on our results, nitrate concentrations increased with the haze aggravating

435   processes (**Fig.2b**), as a positive feedback effect, the elevated nitrate could in turn

436   enhance HONO formation and further enhance the atmospheric oxidation capacity

437   during daytime. Considering J$_{nitrate}$ was still unclear, sensitivity tests were conducted

438   and presented in the discussion section.

439
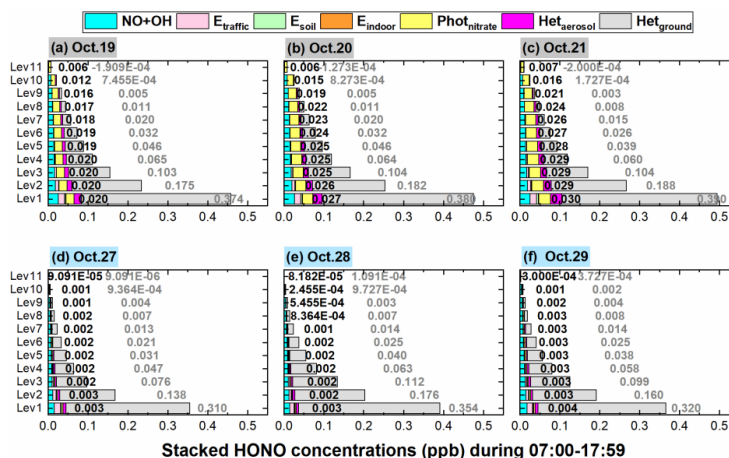
Figure 7 The 95-NCP-site-averaged daytime HONO concentrations at different heights when the NO+OH reaction and the six potential HONO sources were included during a typical haze aggravating process of Oct.19–21 (a–c) and a clean period of Oct.27–29 (d–f) of 2018. The first column numbers in black in each graph are for $Phot_{nitrate}$, and the second column numbers in gray are for Het_{ground}.
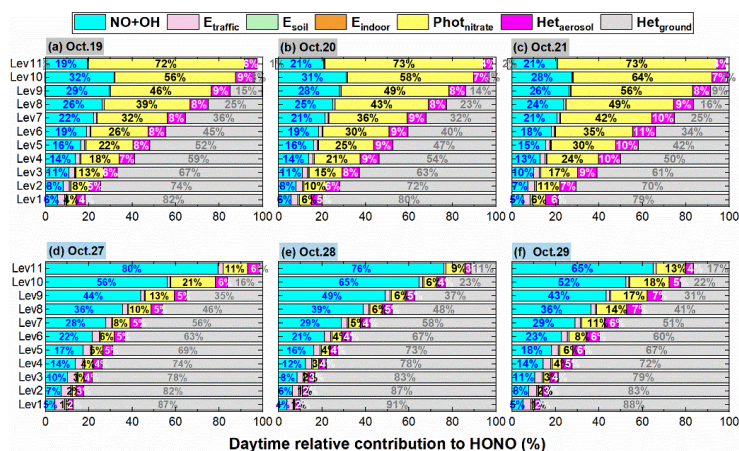
Figure 8 The 95-NCP-site-averaged relative contributions of the NO+OH reaction and each of the six potential HONO sources to daytime HONO concentrations at different heights during a typical

450   haze aggravating process of Oct.19–21 (a–c) and a clean period of Oct.27–29 (d–f) of 2018. The

451   first column numbers in blue in each graph are for the NO+OH reaction, the second column numbers

452   in black are for Phot$_{nitrate}$, the third column numbers in white are for Het$_{aerosol}$, and the fourth column

453   numbers in gray are for Het$_{ground}$.

454

455   **3.3.2 Enhanced OH and its production rate**

456   **Fig.9** demonstrates daytime variations of OH production (P(OH)) and loss (L(OH))

457   rates near the surface and in the vertical-averaged layer (from ground to the height of

458   2.5km) at the 95 NCP sites for the Base and 6S cases during Oct.11–31, 2018. Near the

459   surface, daytime P(OH) and L(OH) were significantly enhanced by~320% for the 6S

460   case (mean was 5.27 ppb h^{-1}) compared with the base case (mean was 1.26 ppb h^{-1}).

461   After adding the six potential HONO sources in case 6S, the daytime P(OH) via HONO

462   and O$_3$ photolysis was 1.81 ppb h^{-1} and 0.10 ppb h^{-1}, respectively, HONO photolysis

463   was the main source of the primary formation of OH, while the secondary formed OH

464   via HO$_2$+NO (3.14 ppb h^{-1}) was the dominant source of the total OH formation.

465   Vertically, daytime P(OH) or L(OH) was enhanced by ~105% for the 6S case (mean

466   was 2.21 ppb h^{-1}) compared with the base case (mean was 1.08 ppb h^{-1}), the daytime

467   P(OH) via the photolysis of HONO and O$_3$ and via the HO$_2$+NO reaction was 0.48 ppb

468   h^{-1}, 0.12 ppb h^{-1} and 1.52 ppb h^{-1}, respectively. In short, the six potential HONO sources

469   accelerated OH production and loss rates remarkably near the surface and noticeably in

470   the considered vertical layers.

471

472
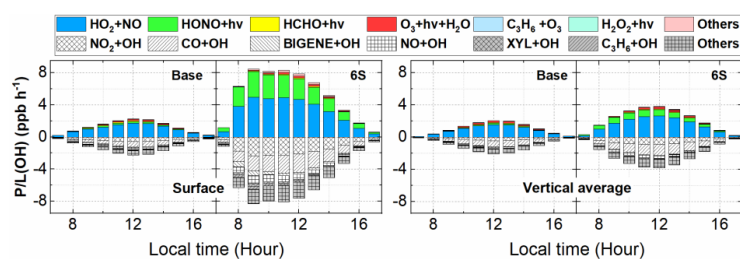
Figure 9 Diurnal mean variations of OH production (P(OH)) and loss (L(OH)) rates including major

production and loss reactions near the surface and in the vertically-averaged layer (from ground to

the height of 2.5km) at the 95 NCP sites for the Base and 6S cases during Oct.11–31, 2018.

476

Fig.10 shows the linear relationships between daytime-averaged P(OH) and PM$_{2.5}$

concentrations and between daytime-averaged OH and PM$_{2.5}$ concentrations from

ground to the height of 2.5km at the 95 NCP sites during Oct. 11–31 of 2018. Both

P(OH) for the two cases (Base and 6S) and the enhanced P(OH) due to the six potential

HONO sources showed a strong positive correlation ($R>0.8$) with PM$_{2.5}$ concentrations

at the 95 NCP sites, and the enhanced P(OH) for the 6S case reached 0.043 ppb h^{-1} per

1μg m^{-3} of a PM$_{2.5}$ enhancement. Similarly, high positive correlation ($R>0.6$) could be

found between OH and PM$_{2.5}$ concentrations, the OH concentrations and enhancements

due to the six potential HONO sources were both higher in hazy days than those in

clean days, and the enhancement of OH reached 3.62×10^4 molec cm^{-3} per μg m^{-3} of

PM$_{2.5}$ for case 6S. These results were consistent with a recent field study reported by

Slater et al. (2020), who found that the OH observed in haze events was elevated in

central Beijing in November–December of 2016. Furthermore, two observations

490 confirmed the key role of HONO in producing primary OH despite the lower photolysis

491 frequency in haze aggravating processes (Slater et al., 2020; Tan et al., 2018), consistent

492 with our simulations (**Fig.S6** shows the relationship between surface $PM_{2.5}$ and

493 photolysis frequencies of NO_2, HONO and HNO_3 in this study).
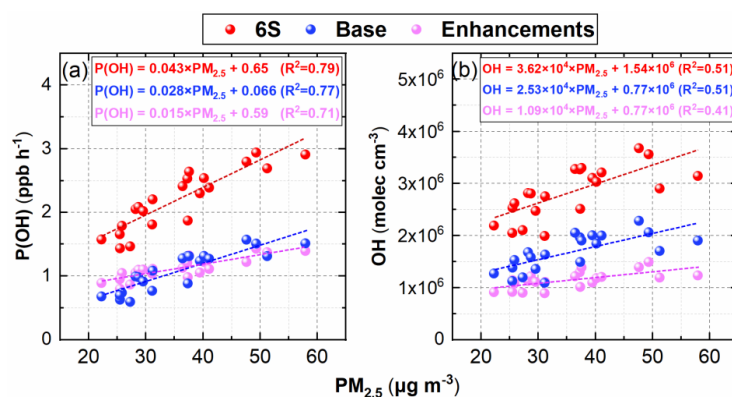
495 **Figure 10** The linear relationships between daytime-averaged P(OH) and $PM_{2.5}$ concentrations (a)

496 and between daytime-averaged OH and $PM_{2.5}$ concentrations (b) from ground to the height of 2.5km

497 at the 95 NCP sites during Oct. 11–31 of 2018.

499 **Fig.11&12** show the detailed comparisons of P(OH) and OH enhancements during

500 a haze aggravating process and a clean period. It can be seen that both P(OH) and OH

501 were enhanced in hazy days compared with clean days, and P(OH) and OH increased

502 with the aggravated haze pollution. Among the six potential HONO sources, Het_{ground}

503 was the largest contributor to the enhanced P(OH) and OH near the surface, but its

504 contribution was relatively stable under different pollution levels and was attenuated

505 rapidly with height in both hazy and clean days; the contribution induced by $Phot_{nitrate}$

506 was remarkably increased in haze aggravating processes and was about one order of

507   magnitude higher than that in clean days; $Het_{aerosol}$ also increased with the pollution

508   levels but with relatively small values, while the impact of other three direct emission

509   sources of HONO was quite small.

510
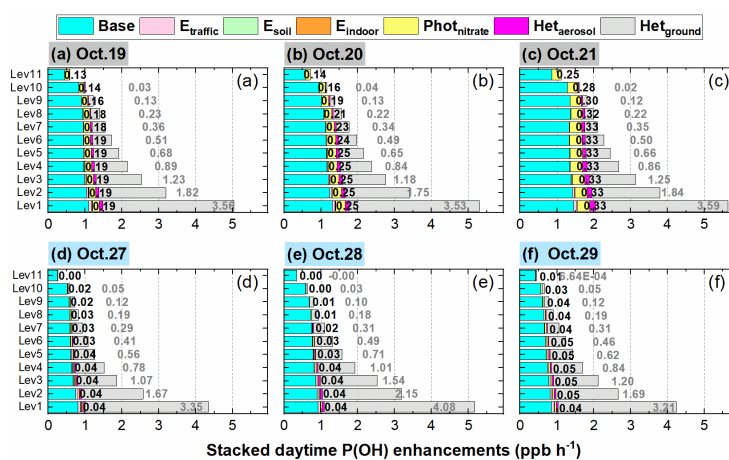
511

512   **Figure 11** The 95-NCP-site-averaged daytime P(OH) for the base case and the enhancements due

513   to the six potential HONO sources during a typical haze aggravating process of Oct.19–21 (a–c)

514   and a clean period of Oct.27–29 (d–f) of 2018. The first column number in black in each graph is

515   for $Phot_{nitrate}$, and the second column number in gray is for Het_{ground}.

516
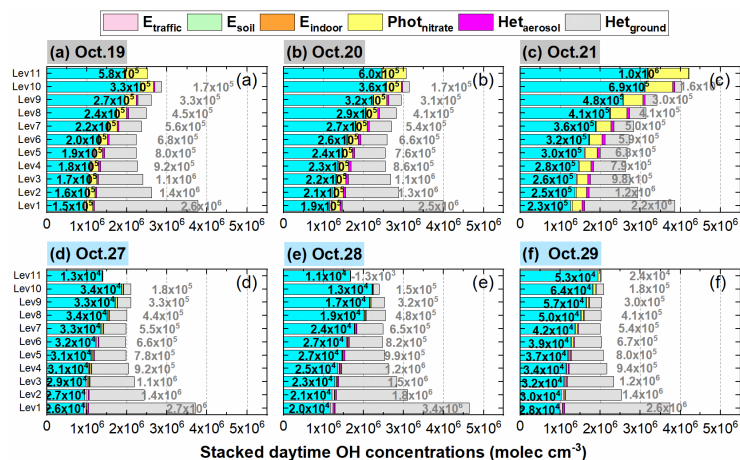
517

518 **Figure 12** The 95-NCP-site-averaged daytime OH concentrations for the base case and the

519 enhancements due to the six potential HONO sources during a typical haze aggravating process of

520 Oct.19–21 (a–c) and a clean period of Oct.27–29 (d–f) of 2018. The first column number in black

521 in each graph is for $Phot_{nitrate}$, and the second column number in gray is for Het_{ground}.

522

523 **3.2.3 Enhanced DMA8 O_3**

524 **Fig.13** demonstrates the linear relationship between DMA8 O_3 enhancements and

525 daytime $PM_{2.5}$ concentrations in each vertical layer (a) and the averaged vertical layer

526 for the considered eleven layers (b) at the 95 NCP sites during Oct. 11–31 of 2018. A

527 good correlation (R>0.8) between DMA8 O_3 enhancements and daytime $PM_{2.5}$

528 concentrations in the vertical averaged layer suggests that the enhanced O_3 due to the

529 six potential HONO sources was larger in polluted days and increased during the haze

530 aggravating processes. The enhanced DMA8 O_3 was < 2ppb when $PM_{2.5}$ was < 20μg

531 m^{-3}, and was >10 ppb when $PM_{2.5}$ was > 60μg m^{-3} on average, with a mean DMA8 O_3

532   enhancement of 0.24 ppb per ug m^{-3} of $PM_{2.5}$.

533
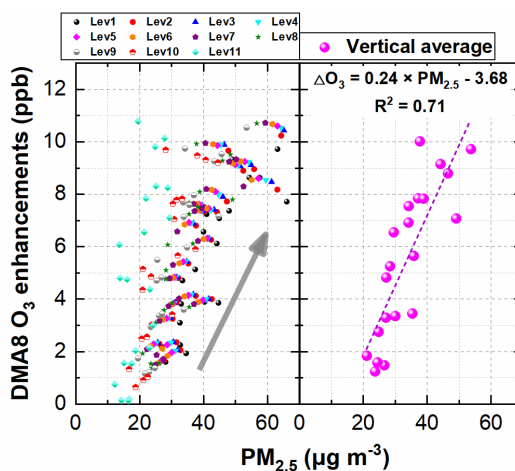
534

535   **Figure 13** The linear relationship between DMA8 O_3 enhancements and daytime $PM_{2.5}$

536   concentrations in each vertical layer (a) and the averaged vertical layer for the considered eleven

537   layers (b) at the 95 NCP sites during Oct. 11–31 of 2018.

538

539   **Fig.14** shows the 95-NCP-site-averaged DMA8 O_3 enhancements due to the six

540   potential HONO sources during a typical haze aggravating process of Oct.19–21 and a

541   clean period of Oct.27–29 of 2018. A significant enhancement of DMA8 O_3 can be

542   found during the haze aggravating process compared with during clean days. The

543   enhanced DMA8 O_3 was ~5.5 ppb (Oct.19), ~ 7 ppb (Oct.20) and ~ 10 ppb (Oct.21),

544   respectively, during the haze aggravating process, while that was usually ~2 ppb in

545   clean days.

546   In clean days, Het_{ground} was the dominant contributor (~1.5–2 ppb) to the enhanced

547   DMA8 O_3 among the six potential HONO sources, the contribution of $Phot_{nitrate}$ to the

548   enhanced DMA8 O_3 was ~0.1–0.4 ppb, while that of the other four sources was minor.

549   When it comes to the comparison between the haze aggravating process (Oct.19–21)

550   and clean days, the DMA8 O_3 enhancements induced by Het_{ground} were doubled and

551   reached ~3–4 ppb; the contribution of $Phot_{nitrate}$ to the enhanced DMA8 O_3 substantially

552   increased and reached ~2–4.5 ppb (Oct.19), ~3–6 ppb (Oct.20) and ~5–10 ppb (Oct.21),

553   respectively; $Het_{aerosol}$ showed an increasing contribution to the enhanced DMA8 O_3

554   during haze aggravating process (~0.3 ppb in Oct.19, ~0.4 ppb in Oct.20 and ~0.7 ppb

555   in Oct.21), while the impacts of the other three direct emission sources ($E_{traffic}$, E_{soil}, and

556   E_{indoor}) on the enhanced DMA8 O_3 were minor.

557
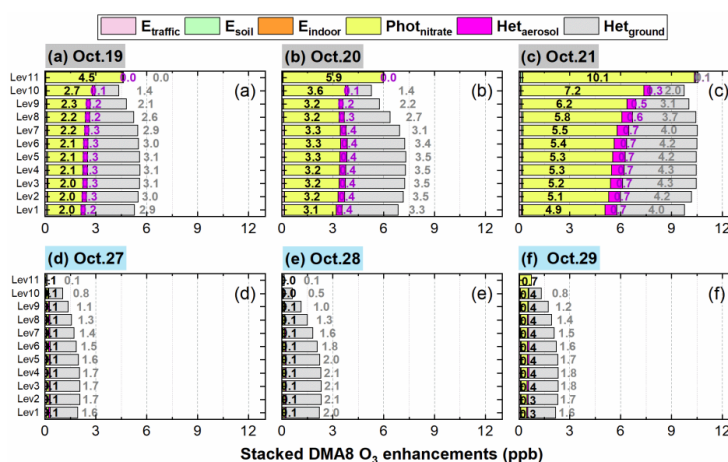
558

559   **Figure 14** The 95-NCP-site-averaged DMA8 O_3 enhancements due to the six potential HONO

560   sources during a typical haze aggravating process of Oct.19–21 (a–c) and a clean period of Oct.27–

561   29 (d–f) of 2018. The column in black numbers in each graph is for $Phot_{nitrate}$, the column in purple

562   numbers in each graph is for $Het_{aerosol}$, and the column in gray numbers is for Het_{ground}.

563

3.4 Vertical variations of O_3-NO_x-VOCs sensitivity

Based on the results above, $Phot_{nitrate}$ could significantly enhance the DMA8 O_3 by

one order of magnitude in the considered vertical layers (especially at elevated heights)

in polluted events, but previous studies have not fully discussed. To better understand

its role in vertical O_3 formation, the O_3-NO_x-VOCs sensitivity was analyzed by using

the $P(H_2O_2)/P(HNO_3)$ ratio proposed by Sillman (1995), which is more suitable than

the concentration ratio of H_2O_2/HNO_3 because of the large dry deposition velocity of

the two gases in the troposphere (Sillman, 1995). A transition point of $P(H_2O_2)/P(HNO_3)$

= 0.35 was suggested by Sillman (1995), when $P(H_2O_2)/P(HNO_3)$ was <0.35, O_3 shows

VOCs-sensitive chemistry (increasing VOC concentrations can significantly elevate O_3

levels) and when $P(H_2O_2)/P(HNO_3)$ was >0.35, O_3 tends to NO_x-sensitive chemistry

(increasing NO_x concentrations can significantly elevate O_3 levels).

Fig.15 demonstrates the 95-NCP-site-averaged $P(H_2O_2)/P(HNO_3)$ ratio at each

vertical layer for the 6S case during a typical haze aggravating process of Oct.19–21

and a clean period of Oct.27–29 of 2018. Obviously opposite O_3 sensitivity appeared

between the lower layers (VOCs sensitive) and the higher layers (NO_x sensitive) in both

clean and hazy days, and the transition point usually appeared at the eighth layer (~600–

800 m).

The nitrate photolysis reaction is assumed to produce HONO and NO_x (Zhou et al.,

2003), this reaction not only enhances OH concentrations via HONO photolysis, but

also directly releases NO_x back into the troposphere. Considering the NO_x-sensitive O_3

chemistry at higher layers (>800m), elevating OH and NO_x concentrations are both

586   favorable for O₃ formation, especially in haze aggravating processes with abundant

587   nitrate (detailed vertically enhanced O₃ production/loss rates induced by Phot$_{nitrate}$ are

588   given in **Fig.S7**).

589
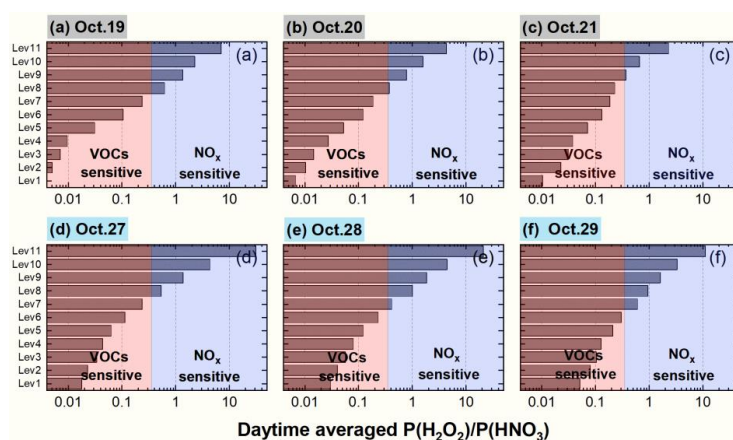
590

591   **Figure 15** The 95-NCP-site-averaged P(H₂O₂)/P(HNO₃) ratio at each vertical layer for the 6S case

592   during a typical haze aggravating process of Oct.19–21 (a–c) and a clean period of Oct.27–29 (d–f)

593   of 2018.

594

595   The specific role of the produced HONO or NO₂ via the nitrate photolysis reaction

596   (R2) in DMA8 O₃ enhancements were further analyzed and is shown in **Fig. 16**, the

597   produced NO₂ and HONO jointly promoted O₃ formation and increased DMA8 O₃

598   concentrations. From the surface to ~1200m (Level 9), the DMA8 O₃ enhancements for

599   case D_HONO was ~5 times those for case D_NO₂, while at ~2000 m (Level 11) the

600   DMA8 O₃ enhancements for case D_HONO was ~2 times those for case D_NO₂. A

601   balance exists between the propagation of the free radical interconversion cycle and the

602   rate of termination of the cycle for the O₃ formation chemistry (Gligorovski et al., 2015),

603 considering the 0.67 and 0.33 yields (ratio is 2) for the two products, we could conclude

604 that the impact of produced HONO on O_3 enhancements was larger than produced NO_2

605 near the surface, while at higher altitude (>2000 m) the impacts of the two products

606 were similar.

607
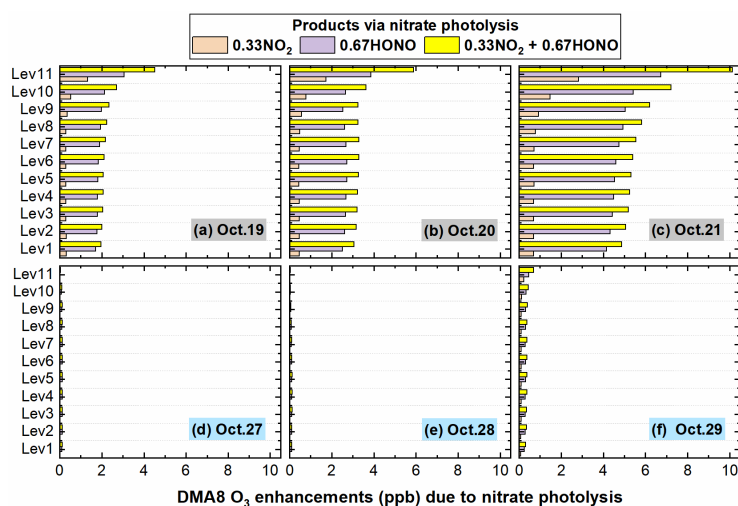
608

609 **Figure 16** The 95-NCP-site-averaged DMA8 O_3 enhancements due to nitrate photolysis with three

610 product scenarios (cases D_NO_2, D_HONO and D) during a typical haze aggravating process of

611 Oct.19–21 (a–c) and a clean period of Oct.27–29 (d–f) in 2018.

612

613 **4. Discussion**

614 **4.1 Vertical variations of potential HONO sources**

615   The relative contribution of potential HONO sources near the surface,

616 corresponding to the first model layer (0 to ~35 m) in our simulation, was quantified in

617   previous modelling studies (Fu et al., 2019; Xue et al., 2020; Zhang et al., 2021),

618   however, for those potential HONO sources, their relative contributions to HONO

619   concentrations near and above the surface should be different. Based on our results

620   (Figs.7&8), the effects of aerosol related HONO sources would be severely

621   underestimated in hazy days when only focused surface HONO, especially for nitrate

622   photolysis. Near the surface in NCP, the daytime contribution of $Phot_{nitrate}$ to HONO

623   concentrations in hazy days was only ~4–6%, but this source contributed ~35–50% of

624   the enhanced DMA8 O_3 (**Fig.14a–c**); above the eighth layer (~800 m), this source

625   contributed ~50–70% of HONO concentrations and ~50–95% of the enhanced DMA8

626   O_3 (**Fig.14a–c**).

627   A recent observation in urban Beijing reported vertical HONO concentrations from

628   three heights above the surface and found that extremely high HONO concentrations

629   occurred at 120 m (~5 ppb) and 240 m (~3 ppb) rather than near the surface (~1.2 ppb)

630   during 12:00 in a typical hazy day (Zhang et al., 2020b). The observation was unusual

631   at noontime under strong convection conditions, inconsistent with those most previous

632   observations indicating a HONO decrease trend with height, especially with the

633   observational results of Zhu et al. (2011) and Meng et al. (2020) and simulated results

634   of Zhang et al. (2021) at the same observational site (including our simulations in

635   **Fig.S5**). The contributions of different HONO sources at each layer were analyzed by

636   using a box model, but ~80–90% of the noontime HONO at higher layers could not be

637   explained by the known HONO formation mechanisms (Zhang et al., 2019c). The box

638   model neglected the vertical convection, so the ground related HONO sources had no

639   contribution to HONO concentrations at the higher layers, thus their HONO simulations

640   were actually underestimated compared with our results and the previous studies of

641   Wong et al. (2011) and Zhang et al. (2021).

642

643   **4.2 Uncertainties of $J_{nitrate}$/J_{HNO3} ratios and their impacts**

644   **4.2.1 Uncertainties of $J_{nitrate}$/J_{HNO3} ratios in DMA8 O_3 enhancements**

645   Based on our results, Het_{ground} and $Phot_{nitrate}$ were the two major contributors to the

646   enhanced DMA8 O_3, especially for $Phot_{nitrate}$ in hazy days with higher $PM_{2.5}$

647   concentrations. The uncertainties of $Phot_{nitrate}$ (four $J_{nitrate}$/J_{HNO3} ratios) in O_3

648   enhancements were analyzed and are shown in **Fig.17** (the uncertainties for Het_{ground}

649   are given in **text S2**). During the haze aggravating process, the enhanced DMA8 O_3

650   increased from ~0.3 to ~0.5 ppb, from ~0.9 to ~2 ppb, from ~2 to ~6 ppb, and from ~5

651   to ~12 ppb, with the $J_{nitrate}$/J_{HNO3} ratio being 1, 7, 30, 120, respectively, and the enhanced

652   O_3 increased with altitude. In clean days, the impact of $Phot_{nitrate}$ on O_3 enhancements

653   was small (<1 ppb) even with a $J_{nitrate}$/J_{HNO3} ratio of 120.

654

655
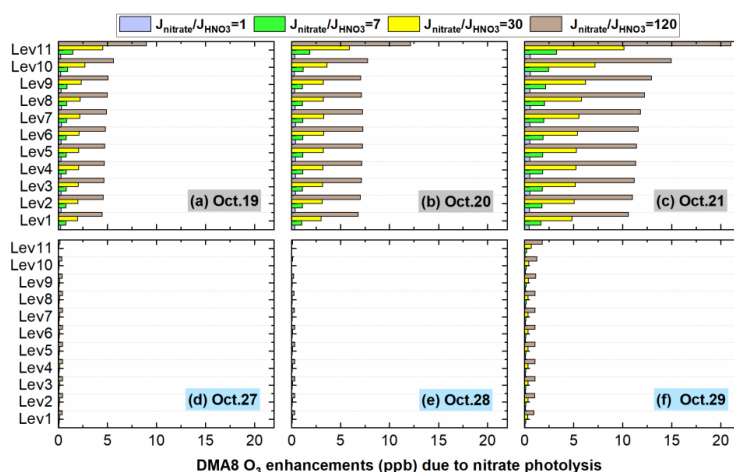
Figure 17 The 95-NCP-site-averaged DMA8 O_3 enhancement induced by nitrate photolysis with

four $J_{nitrate}/J_{HNO3}$ ratios (1, 7, 30 and 120) during a typical haze aggravating process of Oct.19–21

(a–c) and a clean period of Oct.27–29 (d–f) of 2018.

659

4.2.2 Uncertainties of $J_{nitrate}/J_{HNO3}$ ratios in nitrate concentrations

We found considerable enhancements in O_3 concentrations induced by nitrate

photolysis, yet it is still unclear that to what extent nitrate photolysis could influence

nitrate concentrations. The overall nitrate concentrations for the base case and the

nitrate enhancements induced by the potential HONO sources decreased with rising

altitude except for $Phot_{nitrate}$ (**Fig.S8a**). Het_{ground} enhanced nitrate concentrations by ~1.5

$\mu g\ m^{-3}$ near the surface and the enhancements decreased to $< 0.5 \mu g\ m^{-3}$ above the eighth

model layer (~800m); the nitrate enhancements due to $Het_{aerosol}$ and $E_{traffic}$ near the

surface were ~0.2 and ~0.1 $\mu g\ m^{-3}$, respectively, and were < 0.1 and $< 0.04\ \mu g\ m^{-3}$ above

the sixth model layer (~500m). For $Phot_{nitrate}$, the overall impact of four $J_{nitrate}/J_{HNO3}$

670   ratios on nitrate concentrations is shown in **Fig.S8b**, a smaller $J_{nitrate}/J_{HNO3}$ ratio of 1 or

671   7 had a limited impact on nitrate concentrations of ~0–0.05 μg m^{-3}, a $J_{nitrate}/J_{HNO3}$ ratio

672   of 30 slightly decreased nitrate concentrations by ~0.2 μg m^{-3}, while the $J_{nitrate}/J_{HNO3}$

673   ratio of 120 decreased vertical nitrate concentrations by ~0.3–0.8 μg m^{-3}. The relative

674   nitrate changes caused by Phot$_{nitrate}$ were calculated by the differences between four

675   cases added Phot$_{nitrate}$ (cases Nit_1, Nit_7, D and Nit_120) and the base case, the vertical

676   nitrate concentrations were reduced by ~0–0.4% ($J_{nitrate}/J_{HNO3}$=1), ~0–2% (7), ~2–5%

677   (30) and ~10–14% (120) at the 95 NCP sites, meaning that the Phot$_{nitrate}$ impact on

678   vertical nitrate concentrations is limited (<5%) when adopting a relatively small

679    $J_{nitrate}/J_{HNO3}$ ratio (< 30) (**Fig.S8c**).

680   **Fig.18** shows the detailed relative nitrate changes caused by Phot$_{nitrate}$ during a

681   typical haze aggravating process and a clean period (corresponding concentrations were

682   shown in **Fig.S9**), the percentage nitrate reduction was usually smaller in hazy days

683   than in clean days, and nitrate was slightly reduced during the haze aggravating

684   processes, the nitrate reduction was <5% when adopting the $J_{nitrate}/J_{HNO3}$ ratio of 30 both

685   in clean and hazy days.

686

687
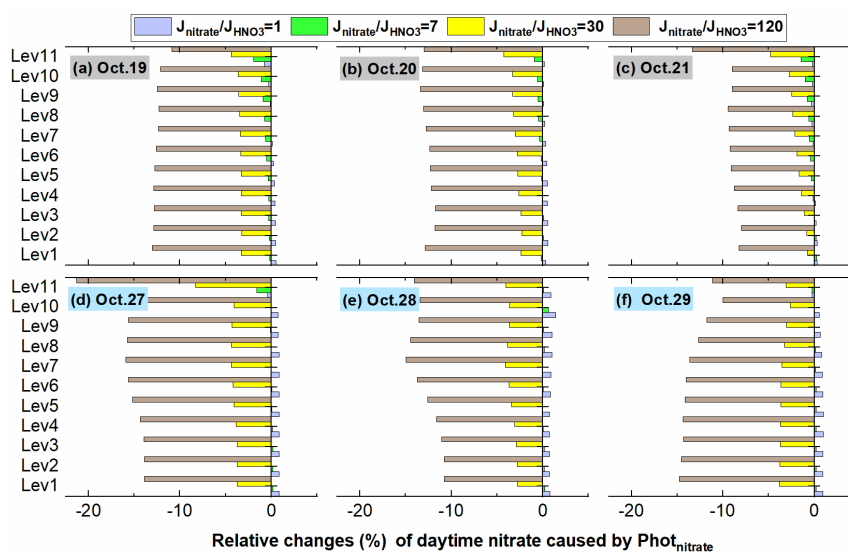
Figure 18 The 95-NCP-site-averaged nitrate relative changes with four $J_{nitrate}/J_{HNO3}$ ratios (1, 7, 30

and 120) compared with the base case (c) during a typical haze aggravating process of Oct.19–21

(a–c) and a clean period of Oct.27–29 (d–f) of 2018.

691

4.2.3 Possible ranges of the $J_{nitrate}/J_{HNO3}$ ratio

From the above discussion, we can find that the enhanced OH and O_3 due to

$Phot_{nitrate}$ are remarkable during haze aggravating processes, and the exact value of the

$J_{nitrate}/J_{HNO3}$ ratio requires more studies.

Fig. 19 shows diurnal patterns of surface-averaged and vertical-averaged

simulations of nitrate photolysis frequency with four different $J_{nitrate}/J_{HNO3}$ ratios at the

95 NCP sites during the study period. The nitrate photolysis frequency at 12:00 was

3.7×10^{-7}, 2.6×10^{-6}, 1.1×10^{-5} and 4.5×10^{-5} s^{-1}, when adopting a $J_{nitrate}/J_{HNO3}$ ratio of 1, 7,

30 and 120, respectively. The corresponding vertical-averaged nitrate photolysis

701 frequency was slightly larger (~10%) and was 4.2×10^{-7}, 2.9×10^{-6}, 1.3×10^{-5} and 5.0×10^{-5} s^{-1}, respectively. Adopting a $J_{nitrate}/J_{HNO3}$ ratio of 30 in the 6S case, with the

702 ^{5} s^{-1}, respectively. Adopting a $J_{nitrate}/J_{HNO3}$ ratio of 30 in the 6S case, with the

703 corresponding $J_{nitrate}$ of $1.1–1.3 \times 10^{-5}$ s^{-1}, produced ~30–50% of the enhanced O_3 near

704 the surface in hazy days (**Fig.13**), and ~70–90% of the enhanced O_3 at higher layers

705 (>800 m).

706   The reported values of $J_{nitrate}$ from previous studies are summarized in **Table 4**. The

707 experimental $J_{nitrate}$ values have been controversial over the past two decades and are

708 still arguable currently. In our simulations for the 6S case, nitrate photolysis contributed

709 from ~1% (clean days) to ~5% (hazy days) to surface HONO during daytime when

710 using the $J_{nitrate}/J_{HNO3}$ ratio of 30 in NCP, consistent with <8% at a rural site in NCP

711 reported by Xue et al. (2020) and ~1% at urban Beijing reported by Zhang et al. (2021)

712 using the same ratio; however, the increasing contribution of nitrate photolysis to

713 HONO concentrations with rising altitude based on our simulations (**Fig.7**), has not

714 been discussed in previous research. Furthermore, we found that the overall impact of

715 nitrate photolysis to OH and O_3 would be severely underestimated when the

716 contribution of nitrate photolysis to vertical HONO was excluded.

717   A larger $J_{nitrate}/J_{HNO3}$ ratio of 120 for nitrate photolysis ($4.5–5.0 \times 10^{-5}$ s^{-1} at 12:00)

718 produced ~25–30% of noontime HONO in NCP in our study (**Fig.S10**), comparable

719 with 30–40% in previous modelling studies (Fu et al., 2019; Shi et al., 2020) when

720 using the $J_{nitrate}/J_{HNO3}$ ratio of 118.57 ($8.3 \times 10^{-5}/ 7 \times 10^{-7}$). In haze aggravating processes,

721 the contribution of $Phot_{nitrate}$ ($J_{nitrate}/J_{HNO3} = 120$) to the DMA8 O_3 enhancements

722 reached ~5–10 ppb near the surface and ~8–20 ppb above the tenth model layer (**Fig.17**),

723   these enhancements were extremely large. In a previous modelling study by Fu et al.

724   (2020), the daytime surface O_3 simulations were systematically overestimated by ~ 5

725   ppb in NCP in winter (**Fig.S4** in Fu et al. (2020)), the inclusion of $Phot_{nitrate}$ ($J_{nitrate}/J_{HNO3}$

726   = 118.57) in their study might cause the overestimation. From the above, a $J_{nitrate}/J_{HNO3}$

727   ratio of 120, or a $J_{nitrate}$ value of ~4–5×10^{-5} s^{-1} is possibly overestimated. When adopting

728   the maximum $J_{nitrate}$ value of 10^{-4} s^{-1} reported by Ye et al. (2016) and Bao et al. (2018),

729   we reasonably speculate that O_3 simulations will be significantly overestimated,

730   especially at higher altitude with NO_x-sensitive O_3 chemistry (**Figs.15**).

731   Romer et al. (2018) and Kasibhatla et al. (2018) suggested that a $J_{nitrate}/J_{HNO3}$ ratio

732   of 30 or smaller would be more suitable, being about the minimum value reported by

733   Ye et al. (2016) and Bao et al. (2018), and has significantly influenced the O_3

734   simulations in haze aggravating processes. The lack of photo-catalyzer in suspended

735   submicron particulate sodium and ammonium nitrate may cause a lower $J_{nitrate}/J_{HNO3}$

736   ratio (<10) reported by Shi et al. (2021), so more chamber experiments need to be

737   conducted by using the particles collected in the real atmosphere. Choosing a larger

738    $J_{nitrate}$ value might cover up other ground-based unknown HONO sources, creating an

739   illusion of good model simulations of daytime HONO, but resulting in overestimation

740   of O_3 concentrations. Considering the uncertainties of NO_x or VOCs emissions, which

741   also significantly impact O_3 simulations, more studies are needed to find the exact value

742   of $J_{nitrate}$ in the real atmosphere.

743

744
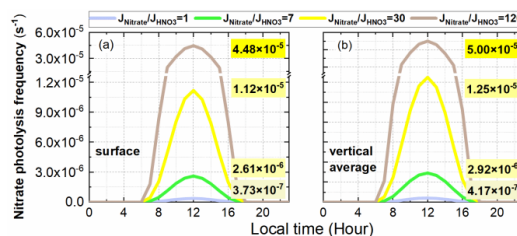
Figure 19 Diurnal patterns of surface-averaged (a) and vertical-averaged (b) simulations of nitrate

photolysis frequency with four different $J_{nitrate}/J_{HNO3}$ ratios (1, 7, 30, 120) at the 95 NCP sites during

the study period (The nitrate photolysis frequencies at 12:00 is shown in each graph).

748
749
750

751 **Table 4.** Summary of studies on the nitrate photolysis frequency ($J_{nitrate}$) (J_{HNO3} denotes the photolysis
752 frequency of gas HNO_3)

Experimental conditions	Main conclusion	Reference
HNO_3 absorbed on Pyrex surface	$J_{nitrate}$ (1.2×10^{-5} s^{-1}) is 1–2 orders of magnitude faster than in the gas and aqueous phases.	(Zhou et al., 2003)
Atmosphere simulation chamber	$J_{nitrate}$ on snow, ground, and glass surfaces, can be excluded in the chamber.	(Rohrer et al., 2005)
HNO_3 absorbed on glass surface	Photolysis frequency of surfaces adsorbed HNO_3 is > 2 orders of magnitude larger than J_{HNO3}.	(Zhu et al., 2008)
Urban grime-coated surface	$J_{nitrate}$ (1.2×10^{-3} s^{-1}) is 4 orders of magnitude faster than in water (10^{-7} s^{-1}).	(Baergen and Donaldson, 2013)
Various natural/artificial surfaces	$J_{nitrate}$ ranges from 6.0×10^{-6} s^{-1} to 3.7×10^{-4} s^{-1}, 1–3 orders of magnitude higher than J_{HNO3}	(Ye et al., 2016)
Adsorbed HNO_3 on glass surfaces	Photolysis frequency of surfaces adsorbed HNO_3 (2.4×10^{-7} s^{-1}) is very low.	(Laufs and Kleffmann, 2016)
Aerosol filter samples	$J_{nitrate}$ ranges from 6.2×10^{-6} s^{-1} to 5.0×10^{-4} s^{-1} with a mean of 1.3×10^{-4} s^{-1}.	(Ye et al., 2017)
Nitrate aerosol in the MBL	$J_{nitrate}$ is ~10 times higher than J_{HNO3}.	(Reed et al., 2017)
$PM_{2.5}$ in Beijing	$J_{nitrate}$ (1.22×10^{-5} s^{-1} to 4.84×10^{-4} s^{-1}) is 1–3 orders of magnitude higher than J_{HNO3}.	(Bao et al., 2018)
Sea-salt particulate nitrate	$J_{nitrate}$ is 25–50 times higher than J_{HNO3}.	(Kasibhatla et al., 2018)

Particles collected on filters	$J_{nitrate}$ is ≤ 30 times J_{HNO3}.	(Romer et al., 2018)
CMAQ simulation	Nitrate photolysis contributed ~30% of noontime HONO with a $J_{nitrate}/J_{HNO3}$ ratio of ~120.	(Fu et al., 2019)
CMAQ simulation	A $J_{nitrate}/J_{HNO3}$ ratio of 100 better improved sulfate simulations than a $J_{nitrate}/J_{HNO3}$ ratio of 10.	(Zheng et al., 2020)
MCM Box model	Nitrate photolysis contribution to HONO was < 8% with a $J_{nitrate}/J_{HNO3}$ ratio of 30.	(Xue et al., 2020)
MCM Box model	Nitrate photolysis contributed ~40% of noontime HONO with a $J_{nitrate}/J_{HNO3}$ ratio of ~120.	(Shi et al., 2020)
Smog chamber	The $J_{nitrate}/J_{HNO3}$ ratio was <10 for suspended submicron $NaNO_3$ and NH_4NO_3.	(Shi et al., 2021)
CMAQ simulation	Nitrate photolysis contribution to surface HONO was ~1.0% with a $J_{nitrate}/J_{HNO3}$ ratio of 30.	(Zhang et al., 2021)
WRF-Chem simulation	The relative contribution of nitrate photolysis to HONO increased with rising altitude and nitrate photolysis contributed the enhanced O_3 much larger in the ABL than near the surface HONO. On average, nitrate photolysis contributed ~5% of surface daytime HONO with a $J_{nitrate}/J_{HNO3}$ ratio of 30 ($\sim1\times10^{-5}$ s^{-1}) but contributed ~30–50% of the enhanced O_3 near the surface in NCP in hazy days.	This study

753   MBL: marine boundary layer; ABL: atmospheric boundary layer.

754

5. Conclusions

In this study, three direct emission sources, the improved NO_2 heterogeneous reactions on aerosol and ground surfaces, and particulate nitrate photolysis in the atmosphere were included into the WRF-Chem to explore the key sources of HONO producing O_3 enhancements during typical autumn haze aggravating processes with co-occurrence of high $PM_{2.5}$ and O_3 in NCP. The six potential HONO sources produced a significant enhancement in surface HONO simulations and improved the mean HONO concentration at the BUCT site to 1.47 ppb from 0.05 ppb (improved the NMB to -14.22% from -97.11% and the IOA to 0.86 from 0.78). The improved HONO significantly enhanced the atmospheric oxidation capacity near the surface and at elevated heights, especially in hazy days, resulting in fast formation of and significant improvements of O_3 during haze aggravating processes in NCP. Although the photolysis frequency is usually lower during hazy days, higher concentrations of NO_2, $PM_{2.5}$ and nitrate favored HONO formation via heterogeneous reactions, leading to stronger atmospheric oxidation capacity. The major results include:

(1) For the surface HONO in NCP, Het_{ground} was the largest source during daytime and nighttime (~50–80%); the contribution of $Phot_{nitrate}$ ($J_{nitrate}/J_{HNO3} = 30$) to surface HONO concentrations was close to that of the NO+OH reaction during daytime (~1–12%) and was ~5% for daytime average; $E_{traffic}$ was important during nighttime (~10–20%) but small during daytime (<5%); the contribution of $Het_{aerosol}$ was minor (~2–3%) in daytime and <10% in nighttime; the contribution of E_{soil} was <3%, and E_{indoor} could be neglected. Vertically, the HONO enhancements due to ground-based potential

777   HONO sources ($E_{traffic}$, E_{soil}, E_{indoor} and Het_{ground}) decreased rapidly with height, while

778   the NO+OH reaction and aerosol-related HONO sources ($Phot_{nitrate}$ and $Het_{aerosol}$)

779   decreased with height much slower. The enhanced HONO due to $Phot_{nitrate}$ in hazy days

780   was about one order of magnitude larger than in clean days and became the dominant

781   HONO source (~30–70% when $J_{nitrate}/J_{HNO3} = 30$) at higher layers, and both HONO

782   concentrations and $Phot_{nitrate}$ contributions increased with the aggravated pollution

783   levels.

784   (2) Near the surface, daytime OH production/loss rates were significantly enhanced

785   by~320% for the 6S case (mean was 5.27 ppb h^{-1}) compared with the base case (mean

786   was 1.26 ppb h^{-1}); vertically, daytime OH production/loss rates were enhanced by ~105%

787   for the 6S case (mean was 2.21 ppb h^{-1}) compared with the base case (mean was 1.08

788   ppb h^{-1}). The enhanced OH production rate and OH due to the six potential HONO

789   sources both showed a strong positive correlation with $PM_{2.5}$ concentrations at the 95

790   NCP sites, with a slope of 0.043 ppb h^{-1}/μg m^{-3} of $PM_{2.5}$ and 3.62×10^4 molec cm^{-3}/μg

791   m^{-3} of $PM_{2.5}$ from the surface to the height of 2.5 km for case 6S, respectively. The

792   atmospheric oxidation capacity (e.g., OH) was enhanced in the haze aggravating

793   process.

794   (3) A strong positive correlation ($r>0.8$) between enhanced O_3 by the six potential

795   HONO sources and $PM_{2.5}$ concentrations was found in NCP, and nitrate photolysis was

796   the largest contributor to the enhanced DMA8 O_3 in hazy days. Vertically, the enhanced

797   DMA8 O_3 was < 2ppb when $PM_{2.5}$ was < 20μg m^{-3}, and that was >10 ppb when $PM_{2.5}$

798   was > 60μg m^{-3} on average, with a slope of 0.24 ppb DMA8 O_3 enhancement /μg m^{-3}

799   of $PM_{2.5}$. The surface enhanced DMA8 O_3 was ~5.5 ppb (Oct.19), ~7 ppb (Oct.20) and

800   ~10 ppb (Oct.21), respectively, during a typical haze aggravating process, while that

801   was usually ~2 ppb in clean days. The contribution of $Phot_{nitrate}$ to the enhanced DMA8

802   O_3 was increased by over one magnitude during the haze aggravating process (up to 5–

803   10 ppb) compared with that in clean days (~0.1–0.5 ppb), and reached ~2–4.5 ppb

804   (Oct.19), ~3–6 ppb (Oct.20) and ~5–10 ppb (Oct.21), respectively, during a typical haze

805   aggravating process vertically.

806   (4) Surface O_3 was controlled by VOCs-sensitive chemistry, while O_3 at higher

807   altitude (>800m) was controlled by NO_x-sensitive chemistry. The nitrate photolysis

808   reaction enhanced OH and NO_x concentrations, both favored O_3 formation at high

809   altitude, especially in haze aggravating processes with abundant nitrate. The produced

810   HONO rather than the produced NO_2 through nitrate photolysis had a stronger

811   promotion for O_3 formation near the surface, but the impacts of the two products on O_3

812   enhancements were similar at higher altitude (~2000 m).

813   (5) Nitrate photolysis only contributed ~5% of the surface HONO in daytime with

814   a $J_{nitrate}/J_{HNO3}$ ratio of 30 (~1×10^{-5} s^{-1}) but contributed ~30–50% of the enhanced O_3 near

815   the surface in NCP in hazy days. The photolysis of nitrate had a limited impact on nitrate

816   concentrations (reduced by <5% with $J_{nitrate}/J_{HNO3}$ =30, and <15% even with a

817    $J_{nitrate}/J_{HNO3}$ ratio of 120), due mainly to the simultaneously enhanced atmospheric

818   oxidation favoring the nitrate formation. Choosing a larger $J_{nitrate}$ value might cover up

819   other ground-based unknown HONO sources, but overestimate vertical sources of

820   HONO, and NO_x and O_3 concentrations, so more studies are still needed to find the

821   exact value of $J_{nitrate}$ in the real atmosphere.

822

823   **Data availability**

824   Data are available upon reasonable request to the corresponding authors.

825

826   **Author contribution:**

827   J.Z., C.L., J.A., M.G, and W.W. conceived and designed the research. J.Z. performed

828   and analyzed WRF-Chem simulations. J.Z., C.L., Y.G., and H.R. performed data

829   analyses and produced the figures. C.L., Y.Z., F.Z., X.F., C.Y., K.D., Y.L., and M.K.,

830   conducted the field observations. W.W., J.A., M.G., Y.L., and M.K. reviewed the article.

831   **Competing interests**

832   The authors declare that they have no conflict of interest.

833

834   **Acknowledgements**

835   This research was partially supported by the National Natural Science Foundation of

836   China (Grant No. 92044302, 42075108, 42107124, 41822703, 91544221, 91844301),

837   Beijing National Laboratory for Molecular Sciences (BNLMS-CXXM-202011) and the

838   China Postdoctoral Science Foundation (grant NO. 2019M660764).

839

References

Alicke, B., Platt, U., Stutz, J., 2002. Impact of nitrous acid photolysis on the total hydroxyl radical budget during the Limitation of Oxidant Production/Pianura Padana Produzione di Ozono study in Milan. J Geophys Res-Atmos 107. doi:10.1029/2000JD000075.

An, J.L., Li, Y., Chen, Y., Li, J., Qu, Y., Tang, Y.J., 2013. Enhancements of major aerosol components due to additional HONO sources in the North China Plain and implications for visibility and haze. Advances in Atmospheric Sciences 30, 57-66.

Avnery, S., Mauzerall, D.L., Liu, J., Horowitz, L.W., 2011a. Global crop yield reductions due to surface ozone exposure: 1. Year 2000 crop production losses and economic damage. Atmospheric Environment 45, 2284-2296.

Avnery, S., Mauzerall, D.L., Liu, J., Horowitz, L.W., 2011b. Global crop yield reductions due to surface ozone exposure: 2. Year 2030 potential crop production losses and economic damage under two scenarios of O_3 pollution. Atmospheric Environment 45, 2297-2309.

Baergen, A.M., Donaldson, D.J., 2013. Photochemical renoxification of nitric acid on real urban grime. Environmental Science & Technology 47, 815-820.

Bao, F., Li, M., Zhang, Y., Chen, C., Zhao, J., 2018. Photochemical Aging of Beijing Urban $PM_{2.5}$: HONO Production. Environmental Science & Technology 52, 6309-6316.

Bao, F.X., Jiang, H.Y., Zhang, Y., Li, M., Ye, C.X., Wang, W.G., Ge, M.F., Chen, C.C., Zhao, J.C., 2020. The Key Role of Sulfate in the Photochemical Renoxification on Real $PM_{2.5}$. Environmental Science & Technology 54, 3121-3128.

Chen, S., Wang, H., Lu, K., Zeng, L., Hu, M., Zhang, Y., 2020a. The trend of surface ozone in Beijing from 2013 to 2019: Indications of the persisting strong atmospheric oxidation capacity. Atmospheric Environment 242, 117801.

Chen, Y., Wang, W.G., Lian, C.F., Peng, C., Zhang, W.Y., Li, J.L., Liu, M.Y., Shi, B., Wang, X.F., Ge, M.F., 2020b. Evaluation and impact factors of indoor and outdoor gas-phase nitrous acid under different environmental conditions. Journal of Environmental Sciences 95, 165-171.

Cui, L., Li, R., Fu, H., Meng, Y., Zhao, Y., Li, Q., Chen, J., 2021. Nitrous acid emission from open burning of major crop residues in mainland China. Atmospheric Environment 244, 117950.

Dong, W., Xing, J., Wang, S., 2010. Temporal and spatial distribution of anthropogenic ammonia emissions in China: 1994-2006. Environmental Sciences (in Chinese) 31, 1457-1463.

Feng, T., Zhao, S., Bei, N., Liu, S., Li, G., 2021. Increasing atmospheric oxidizing capacity weakens emission mitigation effort in Beijing during autumn haze events. Chemosphere 281, 130855.

Feng, Z., De Marco, A., Anav, A., Gualtieri, M., Sicard, P., Tian, H., Fornasier, F., Tao, F., Guo, A., Paoletti, E., 2019. Economic losses due to ozone impacts on human health, forest productivity and crop yield across China. Environ Int 131, 104966.

Feng, Z., Hu, E., Wang, X., Jiang, L., Liu, X., 2015. Ground-level O_3 pollution and its impacts on food crops in China: a review. Environ Pollut 199, 42-48.

Finlayson-Pitts, B.J., Wingen, L.M., Sumner, A.L., Syomin, D., Ramazan, K.A., 2003. The heterogeneous hydrolysis of NO_2 in laboratory systems and in outdoor and indoor atmospheres: An integrated mechanism. Physical Chemistry Chemical Physics 5, 223-242.

Fu, X., Wang, T., Gao, J., Wang, P., Liu, Y.M., Wang, S.X., Zhao, B., Xue, L.K., 2020. Persistent Heavy Winter Nitrate Pollution Driven by Increased Photochemical Oxidants in Northern China.

882   Environmental Science & Technology 54, 3881-3889.

883   Fu, X., Wang, T., Zhang, L., Li, Q.Y., Wang, Z., Xia, M., Yun, H., Wang, W.H., Yu, C., Yue, D.L., Zhou,
884   Y., Zheng, J.Y., Han, R., 2019. The significant contribution of HONO to secondary pollutants during
885   a severe winter pollution event in southern China. Atmospheric Chemistry and Physics 19, 1-14.

886   Gao, W., Tan, G., Hong, Y., Li, M., Nian, H., Guo, C., Huang, Z., Fu, Z., Dong, J., Xu, X., 2013.
887   Development of portable single photon ionization time-of-flight mass spectrometer combined with
888   membrane inlet. International Journal of Mass Spectrometry 334, 8-12.

889   Ge, M., Tong, S., Wang, W., Zhang, W., Chen, M., Peng, C., Li, J., Zhou, L., Chen, Y., Liu, M., 2021.
890   Important Oxidants and Their Impact on the Environmental Effects of Aerosols. The journal of
891   physical chemistry. A.125,3813-3825.

892   Ge, S., Wang, G., Zhang, S., Li, D., Xie, Y., Wu, C., Yuan, Q., Chen, J., Zhang, H., 2019. Abundant NH_3
893   in China Enhances Atmospheric HONO Production by Promoting the Heterogeneous Reaction of
894   SO_2 with NO_2. Environmental Science & Technology 53, 14339-14347.

895   Gligorovski, S., Strekowski, R., Barbati, S., Vione, D., 2015. Environmental Implications of Hydroxyl
896   Radicals ($^{\cdot}$OH). Chem Rev 115, 13051-13092.

897   Gómez Alvarez, E., Sörgel, M., Gligorovski, S., Bassil, S., Bartolomei, V., Coulomb, B., Zetzsch, C.,
898   Wortham, H., 2014. Light-induced nitrous acid (HONO) production from NO_2 heterogeneous
899   reactions on household chemicals. Atmospheric Environment 95, 391-399.

900   Guenther, A.B., Jiang, X., Heald, C.L., Sakulyanontvittaya, T., Duhl, T., Emmons, L.K., Wang, X., 2012.
901   The Model of Emissions of Gases and Aerosols from Nature version 2.1 (MEGAN2.1): an extended
902   and updated framework for modeling biogenic emissions. Geoscientific Model Development 5,
903   1471-1492.

904   Guo, Y., Zhang, J., An, J., Qu, Y., Liu, X., Sun, Y., Chen, Y., 2020. Effect of vertical parameterization of
905   a missing daytime source of HONO on concentrations of HONO, O_3 and secondary organic aerosols
906   in eastern China. Atmospheric Environment 226, 117208.

907   Hendrick, F., Muller, J.F., Clemer, K., Wang, P., De Maziere, M., Fayt, C., Gielen, C., Hermans, C., Ma,
908   J.Z., Pinardi, G., Stavrakou, T., Vlemmix, T., Van Roozendael, M., 2014. Four years of ground-
909   based MAX-DOAS observations of HONO and NO_2 in the Beijing area. Atmospheric Chemistry
910   and Physics 14, 765-781.

911   Huang, X., Li, M.M., Li, J.F., Song, Y., 2012. A high-resolution emission inventory of crop burning in
912   fields in China based on MODIS Thermal Anomalies/Fire products. Atmospheric Environment 50,
913   9-15.

914   Kasibhatla, P., Sherwen, T., Evans, M.J., Carpenter, L.J., Reed, C., Alexander, B., Chen, Q.J., Sulprizio,
915   M.P., Lee, J.D., Read, K.A., Bloss, W., Crilley, L.R., Keene, W.C., Pszenny, A.A.P., Hodzic, A.,
916   2018. Global impact of nitrate photolysis in sea-salt aerosol on NO_x, OH, and O_3 in the marine
917   boundary layer. Atmospheric Chemistry and Physics 18, 11185-11203.

918   Kim, S., VandenBoer, T.C., Young, C.J., Riedel, T.P., Thornton, J.A., Swarthout, B., Sive, B., Lerner, B.,
919   Gilman, J.B., Warneke, C., Roberts, J.M., Guenther, A., Wagner, N.L., Dube, W.P., Williams, E.,
920   Brown, S.S., 2014. The primary and recycling sources of OH during the NACHTT-2011 campaign:
921   HONO as an important OH primary source in the wintertime. J Geophys Res-Atmos 119, 6886-
922   6896.

923   Kleffmann, J., Kurtenbach, R., Lorzer, J., Wiesen, P., Kalthoff, N., Vogel, B., Vogel, H., 2003. Measured
924   and simulated vertical profiles of nitrous acid - Part I: Field measurements. Atmospheric
925   Environment 37, 2949-2955.

926   Klosterkother, A., Kurtenbach, R., Wiesen, P., Kleffmann, J., 2021. Determination of the emission indices
927   for NO, NO_2, HONO, HCHO, CO, and particles emitted from candles. Indoor Air 31, 116-127.
928   Kramer, L.J., Crilley, L.R., Adams, T.J., Ball, S.M., Pope, F.D., Bloss, W.J., 2020. Nitrous acid (HONO)
929   emissions under real-world driving conditions from vehicles in a UK road tunnel. Atmospheric
930   Chemistry and Physics 20, 5231-5248.
931   Kubota, M., Asami, T., 1985. Volatilization of Nitrous-Acid from Upland Soils. Soil Science and Plant
932   Nutrition 31, 27-34.
933   Kurtenbach, R., Becker, K.H., Gomes, J.A.G., Kleffmann, J., Lorzer, J.C., Spittler, M., Wiesen, P.,
934   Ackermann, R., Geyer, A., Platt, U., 2001. Investigations of emissions and heterogeneous formation
935   of HONO in a road traffic tunnel. Atmospheric Environment 35, 3385-3394.
936   Laufs, S., Kleffmann, J., 2016. Investigations on HONO formation from photolysis of adsorbed HNO_3
937   on quartz glass surfaces. Physical Chemistry Chemical Physics 18, 9616-9625.
938   Li, G., Lei, W., Zavala, M., Volkamer, R., Dusanter, S., Stevens, P., Molina, L.T., 2010. Impacts of HONO
939   sources on the photochemistry in Mexico City during the MCMA-2006/MILAGO Campaign.
940   Atmospheric Chemistry and Physics 10, 6551-6567.
941   Li, K., Jacob, D.J., Shen, L., Lu, X., De Smedt, I., Liao, H., 2020. Increases in surface ozone pollution
942   in China from 2013 to 2019: anthropogenic and meteorological influences. Atmospheric Chemistry
943   and Physics 20, 11423-11433.
944   Li, L., Chen, C.H., Huang, C., Huang, H.Y., Zhang, G.F., Wang, Y.J., Wang, H.L., Lou, S.R., Qiao, L.P.,
945   Zhou, M., Chen, M.H., Chen, Y.R., Streets, D.G., Fu, J.S., Jang, C.J., 2012. Process analysis of
946   regional ozone formation over the Yangtze River Delta, China using the Community Multi-scale
947   Air Quality modeling system. Atmospheric Chemistry and Physics 12, 10971-10987.
948   Li, M., Zhang, Q., Kurokawa, J., Woo, J.H., He, K.B., Lu, Z.F., Ohara, T., Song, Y., Streets, D.G.,
949   Carmichael, G.R., Cheng, Y.F., Hong, C.P., Huo, H., Jiang, X.J., Kang, S.C., Liu, F., Su, H., Zheng,
950   B., 2017. MIX: a mosaic Asian anthropogenic emission inventory under the international
951   collaboration framework of the MICS-Asia and HTAP. Atmospheric Chemistry and Physics 17,
952   935-963.
953   Li, Y., An, J.L., Min, M., Zhang, W., Wang, F., Xie, P.H., 2011. Impacts of HONO sources on the air
954   quality in Beijing, Tianjin and Hebei Province of China. Atmospheric Environment 45, 4735-4744.
955   Liao, S., Zhang, J., Yu, F., Zhu, M., Liu, J., Ou, J., Dong, H., Sha, Q., Zhong, Z., Xie, Y., Luo, H., Zhang,
956   L., Zheng, J., 2021. High Gaseous Nitrous Acid (HONO) Emissions from Light-Duty Diesel
957   Vehicles. Environmental science & technology 55, 200-208.
958   Lin, Y.L., Farley, R.D., Orville, H.D., 1983. Bulk Parameterization of the Snow Field in a Cloud Model.
959   J Clim Appl Meteorol 22, 1065-1092.
960   Liu, J., Li, S., Zeng, J., Mekic, M., Yu, Z., Zhou, W., Loisel, G., Gandolfo, A., Song, W., Wang, X., Zhou,
961   Z., Herrmann, H., Li, X., Gligorovski, S., 2019. Assessing indoor gas phase oxidation capacity
962   through real-time measurements of HONO and NO_x in Guangzhou, China. Environ Sci Process
963   Impacts 21, 1393-1402.
964   Liu, Z., Wang, Y., Costabile, F., Amoroso, A., Zhao, C., Huey, L.G., Stickel, R., Liao, J., Zhu, T., 2014.
965   Evidence of aerosols as a media for rapid daytime HONO production over China. Environmental
966   Science & Technology 48, 14386-14391.
967   Lu, X., Zhang, L., Wang, X.L., Gao, M., Li, K., Zhang, Y.Z., Yue, X., Zhang, Y.H., 2020. Rapid Increases
968   in Warm-Season Surface Ozone and Resulting Health Impact in China Since 2013. Environmental
969   Science & Technology Letters 7, 240-247.

970   Ma, J., Liu, Y., Han, C., Ma, Q., Liu, C., He, H., 2013. Review of heterogeneous photochemical reactions
971   of NOy on aerosol — A possible daytime source of nitrous acid (HONO) in the atmosphere. Journal
972   of Environmental Sciences 25, 326-334.
973   Ma, Z.Q., Xu, J., Quan, W.J., Zhang, Z.Y., Lin, W.L., Xu, X.B., 2016. Significant increase of surface
974   ozone at a rural site, north of eastern China. Atmospheric Chemistry and Physics 16, 3969-3977.
975   Maji, K.J., Namdeo, A., 2021. Continuous increases of surface ozone and associated premature mortality
976   growth in China during 2015-2019. Environ Pollut 269, 116183.
977   Marion, A., Morin, J., Gandolfo, A., Ormeno, E., D'Anna, B., Wortham, H., 2021. Nitrous acid formation
978   on Zea mays leaves by heterogeneous reaction of nitrogen dioxide in the laboratory. Environ Res
979   193, 110543.
980   Meng, F.H., Qin, M., Tang, K., Duan, J., Fang, W., Liang, S.X., Ye, K.D., Xie, P.H., Sun, Y.L., Xie, C.H.,
981   Ye, C.X., Fu, P.Q., Liu, J.G., Liu, W.Q., 2020. High-resolution vertical distribution and sources of
982   HONO and NO_2 in the nocturnal boundary layer in urban Beijing, China. Atmospheric Chemistry
983   and Physics 20, 5071-5092.
984   Mills, G., Buse, A., Gimeno, B., Bermejo, V., Holland, M., Emberson, L., Pleijel, H., 2007. A synthesis
985   of AOT40-based response functions and critical levels of ozone for agricultural and horticultural
986   crops. Atmospheric Environment 41, 2630-2643.
987   Mills, G., Sharps, K., Simpson, D., Pleijel, H., Broberg, M., Uddling, J., Jaramillo, F., Davies, W.J.,
988   Dentener, F., Van den Berg, M., Agrawal, M., Agrawal, S.B., Ainsworth, E.A., Buker, P., Emberson,
989   L., Feng, Z., Harmens, H., Hayes, F., Kobayashi, K., Paoletti, E., Van Dingenen, R., 2018. Ozone
990   pollution will compromise efforts to increase global wheat production. Glob Chang Biol 24, 3560-
991   3574.
992   Oswald, R., Behrendt, T., Ermel, M., Wu, D., Su, H., Cheng, Y., Breuninger, C., Moravek, A., Mougin,
993   E., Delon, C., Loubet, B., Pommerening-Roser, A., Sorgel, M., Poschl, U., Hoffmann, T., Andreae,
994   M.O., Meixner, F.X., Trebs, I., 2013. HONO emissions from soil bacteria as a major source of
995   atmospheric reactive nitrogen. Science 341, 1233-1235.
996   Perner, D., Platt, U., 1979. Detection of nitrous acid in the atmospeere by differential optical absorption.
997   Geophysical Research Letters 6, 917-920.
998   Pitts, J.N., Wallington, T.J., Biermann, H.W., Winer, A.M., 1985. Identification and Measurement of
999   Nitrous-Acid in an Indoor Environment. Atmospheric Environment 19, 763-767.
1000   Reed, C., Evans, M.J., Crilley, L.R., Bloss, W.J., Sherwen, T., Read, K.A., Lee, J.D., Carpenter, L.J.,
1001   2017. Evidence for renoxification in the tropical marine boundary layer. Atmospheric Chemistry
1002   and Physics 17, 4081-4092.
1003   Richards, B.L., Middleton, J.T., Hewitt, W.B., 1958. Air Pollution With Relation to Agronomic Crops: V.
1004   Oxidant Stipple of Grape. Agronomy Journal 50, 559-561.
1005   Rohrer, F., Bohn, B., Brauers, T., Bruning, D., Johnen, F.J., Wahner, A., Kleffmann, J., 2005.
1006   Characterisation of the photolytic HONO-source in the atmosphere simulation chamber SAPHIR.
1007   Atmospheric Chemistry and Physics 5, 2189-2201.
1008   Romer, P.S., Wooldridge, P.J., Crounse, J.D., Kim, M.J., Wennberg, P.O., Dibb, J.E., Scheuer, E., Blake,
1009   D.R., Meinardi, S., Brosius, A.L., Thames, A.B., Miller, D.O., Brune, W.H., Hall, S.R., Ryerson,
1010   T.B., Cohen, R.C., 2018. Constraints on Aerosol Nitrate Photolysis as a Potential Source of HONO
1011   and NOx. Environmental Science & Technology 52, 13738-13746.
1012   Rondon, A., Sanhueza, E., 1989. High HONO atmospheric concentrations during vegetation burning in
1013   the tropical savannah. Tellus Ser. B-Chem. Phys. Meteorol. 41, 474-477.

1014   Ryan, R.G., Rhodes, S., Tully, M., Wilson, S., Jones, N., Friess, U., Schofield, R., 2018. Daytime HONO,
1015   NO$_2$ and aerosol distributions from MAX-DOAS observations in Melbourne. Atmospheric
1016   Chemistry and Physics 18, 13969-13985.

1017   Sakamaki, F., Hatakeyama, S., Akimoto, H., 1983. Formation of Nitrous-Acid and Nitric-Oxide in the
1018   Heterogeneous Dark Reaction of Nitrogen-Dioxide and Water-Vapor in a Smog Chamber.
1019   International Journal of Chemical Kinetics 15, 1013-1029.

1020   Sarwar, G., Roselle, S.J., Mathur, R., Appel, W., Dennis, R.L., Vogel, B., 2008. A comparison of CMAQ
1021   HONO predictions with observations from the northeast oxidant and particle study. Atmospheric
1022   Environment 42, 5760-5770.

1023   Selin, N.E., Wu, S., Nam, K.M., Reilly, J.M., Paltsev, S., Prinn, R.G., Webster, M.D., 2009. Global health
1024   and economic impacts of future ozone pollution. Environmental Research Letters 4, 044014.

1025   Shi, Q., Tao, Y., Krechmer, J.E., Heald, C.L., Murphy, J.G., Kroll, J.H., Ye, Q., 2021. Laboratory
1026   Investigation of Renoxification from the Photolysis of Inorganic Particulate Nitrate. Environmental
1027   science & technology.

1028   Shi, X., Ge, Y., Zheng, J., Ma, Y., Ren, X., Zhang, Y., 2020. Budget of nitrous acid and its impacts on
1029   atmospheric oxidative capacity at an urban site in the central Yangtze River Delta region of China.
1030   Atmospheric Environment 238, 117725.

1031   Sillman, S., 1995. The use of NO$_y$, H$_2$O$_2$, and HNO$_3$ as indicators for ozone-NO$_x$-hydrocarbon sensitivity
1032   in urban locations. Journal of Geophysical Research: Atmospheres 100, 14175-14188.

1033   Slater, E.J., Whalley, L.K., Woodward-Massey, R., Ye, C.X., Lee, J.D., Squires, F., Hopkins, J.R.,
1034   Dunmore, R.E., Shaw, M., Hamilton, J.F., Lewis, A.C., Crilley, L.R., Kramer, L., Bloss, W., Vu, T.,
1035   Sun, Y.L., Xu, W.Q., Yue, S.Y., Ren, L.J., Acton, W.J.F., Hewitt, C.N., Wang, X.M., Fu, P.Q., Heard,
1036   D.E., 2020. Elevated levels of OH observed in haze events during wintertime in central Beijing.
1037   Atmospheric Chemistry and Physics 20, 14847-14871.

1038   Sorgel, M., Trebs, I., Serafimovich, A., Moravek, A., Held, A., Zetzsch, C., 2011. Simultaneous HONO
1039   measurements in and above a forest canopy: influence of turbulent exchange on mixing ratio
1040   differences. Atmospheric Chemistry and Physics 11, 841-855.

1041   Tan, Z.F., Rohrer, F., Lu, K.D., Ma, X.F., Bohn, B., Broch, S., Dong, H.B., Fuchs, H., Gkatzelis, G.I.,
1042   Hofzumahaus, A., Holland, F., Li, X., Liu, Y., Liu, Y.H., Novelli, A., Shao, M., Wang, H.C., Wu,
1043   Y.S., Zeng, L.M., Hu, M., Kiendler-Scharr, A., Wahner, A., Zhang, Y.H., 2018. Wintertime
1044   photochemistry in Beijing: observations of ROx radical concentrations in the North China Plain
1045   during the BEST-ONE campaign. Atmospheric Chemistry and Physics 18, 12391-12411.

1046   Tang, M.J., Huang, X., Lu, K.D., Ge, M.F., Li, Y.J., Cheng, P., Zhu, T., Ding, A.J., Zhang, Y.H.,
1047   Gligorovski, S., Song, W., Ding, X., Bi, X.H., Wang, X.M., 2017. Heterogeneous reactions of
1048   mineral dust aerosol: implications for tropospheric oxidation capacity. Atmospheric Chemistry and
1049   Physics 17, 11727-11777.

1050   Tang, Y., An, J., Wang, F., Li, Y., Qu, Y., Chen, Y., Lin, J., 2015. Impacts of an unknown daytime HONO
1051   source on the mixing ratio and budget of HONO, and hydroxyl, hydroperoxyl, and organic peroxy
1052   radicals, in the coastal regions of China. Atmospheric Chemistry and Physics 15, 9381-9398.

1053   Theys, N., Volkamer, R., Mueller, J.F., Zarzana, K.J., Kille, N., Clarisse, L., De Smedt, I., Lerot, C.,
1054   Finkenzeller, H., Hendrick, F., Koenig, T.K., Lee, C.F., Knote, C., Yu, H., Van Roozendael, M., 2020.
1055   Global nitrous acid emissions and levels of regional oxidants enhanced by wildfires. Nature
1056   Geoscience 13, 681-686.

1057   Tie, X., Long, X., Li, G., Zhao, S., Cao, J., Xu, J., 2019. Ozone enhancement due to the photodissociation

1058   of nitrous acid in eastern China. Atmospheric Chemistry and Physics 19, 11267-11278.

1059   VandenBoer, T.C., Brown, S.S., Murphy, J.G., Keene, W.C., Young, C.J., Pszenny, A.A.P., Kim, S.,
1060   Warneke, C., de Gouw, J.A., Maben, J.R., Wagner, N.L., Riedel, T.P., Thornton, J.A., Wolfe, D.E.,
1061   Dube, W.P., Ozturk, F., Brock, C.A., Grossberg, N., Lefer, B., Lerner, B., Middlebrook, A.M.,
1062   Roberts, J.M., 2013. Understanding the role of the ground surface in HONO vertical structure: High
1063   resolution vertical profiles during NACHTT-11. J Geophys Res-Atmos 118, 10155-10171.

1064   Villena, G., Kleffmann, J., Kurtenbach, R., Wiesen, P., Lissi, E., Rubio, M.A., Croxatto, G., Rappenglück,
1065   B., 2011. Vertical gradients of HONO, NO$_x$ and O$_3$ in Santiago de Chile. Atmospheric Environment
1066   45, 3867-3873.

1067   Wang, F., An, J.L., Li, Y., Tang, Y.J., Lin, J., Qu, Y., Chen, Y., Zhang, B., Zhai, J., 2014. Impacts of
1068   uncertainty in AVOC emissions on the summer RO$_x$ budget and ozone production rate in the three
1069   most rapidly-developing economic growth regions of China. Advances in Atmospheric Sciences 31,
1070   1331-1342.

1071   Wang, X., Zhang, Y., Hu, Y., Zhou, W., Lu, K., Zhong, L., Zeng, L., Shao, M., Hu, M., Russell, A.G.,
1072   2010. Process analysis and sensitivity study of regional ozone formation over the Pearl River Delta,
1073   China, during the PRIDE-PRD2004 campaign using the Community Multiscale Air Quality
1074   modeling system. Atmospheric Chemistry and Physics 10, 4423-4437.

1075   Wang, Y., Apituley, A., Bais, A., Beirle, S., Benavent, N., Borovski, A., Bruchkouski, I., Chan, K.L.,
1076   Donner, S., Drosoglou, T., Finkenzeller, H., Friedrich, M.M., Friess, U., Garcia-Nieto, D., Gomez-
1077   Martin, L., Hendrick, F., Hilboll, A., Jin, J.L., Johnston, P., Koenig, T.K., Kreher, K., Kumar, V.,
1078   Kyuberis, A., Lampel, J., Liu, C., Liu, H.R., Ma, J.Z., Polyansky, O.L., Postylyakov, O., Querel, R.,
1079   Saiz-Lopez, A., Schmitt, S., Tian, X., Tirpitz, J.L., Van Roozendael, M., Volkamer, R., Wang, Z.R.,
1080   Xie, P.H., Xing, C.Z., Xu, J., Yela, M., Zhang, C.X., Wagner, T., 2020. Inter-comparison of MAX-
1081   DOAS measurements of tropospheric HONO slant column densities and vertical profiles during the
1082   CINDI-2 campaign. Atmospheric Measurement Techniques 13, 5087-5116.

1083   Wang, Y., Dörner, S., Donner, S., Böhnke, S., De Smedt, I., Dickerson, R.R., Dong, Z., He, H., Li, Z., Li,
1084   Z., Li, D., Liu, D., Ren, X., Theys, N., Wang, Y., Wang, Y., Wang, Z., Xu, H., Xu, J., Wagner, T.,
1085   2019. Vertical profiles of NO$_2$, SO$_2$, HONO, HCHO, CHOCHO and aerosols derived from MAX-
1086   DOAS measurements at a rural site in the central western North China Plain and their relation to
1087   emission sources and effects of regional transport. Atmospheric Chemistry and Physics 19, 5417-
1088   5449.

1089   Wilkinson, S., Mills, G., Illidge, R., Davies, W.J., 2012. How is ozone pollution reducing our food supply?
1090   J Exp Bot 63, 527-536.

1091   Wong, K.W., Oh, H.J., Lefer, B.L., Rappengluck, B., Stutz, J., 2011. Vertical profiles of nitrous acid in
1092   the nocturnal urban atmosphere of Houston, TX. Atmospheric Chemistry and Physics 11, 3595-
1093   3609.

1094   Wong, K.W., Tsai, C., Lefer, B., Haman, C., Grossberg, N., Brune, W.H., Ren, X., Luke, W., Stutz, J.,
1095   2012. Daytime HONO vertical gradients during SHARP 2009 in Houston, TX. Atmospheric
1096   Chemistry and Physics 12, 635-652.

1097   Wu, D., Horn, M.A., Behrendt, T., Muller, S., Li, J., Cole, J.A., Xie, B., Ju, X., Li, G., Ermel, M., Oswald,
1098   R., Frohlich-Nowoisky, J., Hoor, P., Hu, C., Liu, M., Andreae, M.O., Poschl, U., Cheng, Y., Su, H.,
1099   Trebs, I., Weber, B., Sorgel, M., 2019. Soil HONO emissions at high moisture content are driven by
1100   microbial nitrate reduction to nitrite: tackling the HONO puzzle. ISME J 13, 1688-1699.

1101   Xing, C., Liu, C., Hu, Q., Fu, Q., Wang, S., Lin, H., Zhu, Y., Wang, S., Wang, W., Javed, Z., 2021. Vertical

1102   distributions of wintertime atmospheric nitrogenous compounds and the corresponding OH radicals
1103   production in Leshan, southwest China. Journal of Environmental Sciences 105, 44-55.

1104 Xing, L., Wu, J.R., Elser, M., Tong, S.R., Liu, S.X., Li, X., Liu, L., Cao, J.J., Zhou, J.M., El-Haddad, I.,
1105   Huang, R.J., Ge, M.F., Tie, X.X., Prevot, A.S.H., Li, G.H., 2019. Wintertime secondary organic
1106   aerosol formation in Beijing-Tianjin-Hebei (BTH): contributions of HONO sources and
1107   heterogeneous reactions. Atmospheric Chemistry and Physics 19, 2343-2359.

1108 Xu, J., Zhang, Y.H., Wang, W., 2006. Numerical study on the impacts of heterogeneous reactions on
1109   ozone formation in the Beijing urban area. Advances in Atmospheric Sciences 23, 605-614.

1110 Xu, W., Yang, W., Han, C., Yang, H., Xue, X., 2021. Significant influences of TiO2 crystal structures on
1111 NO_2 and HONO emissions from the nitrates photolysis. Journal of Environmental Sciences 102,
1112   198-206.

1113 Xue, C., Zhang, C., Ye, C., Liu, P., Catoire, V., Krysztofiak, G., Chen, H., Ren, Y., Zhao, X., Wang, J.,
1114   Zhang, F., Zhang, C., Zhang, J., An, J., Wang, T., Chen, J., Kleffmann, J., Mellouki, A., Mu, Y.,
1115   2020. HONO Budget and Its Role in Nitrate Formation in the Rural North China Plain.
1116   Environmental Science & Technology 54, 11048-11057.

1117 Xue, C.Y., Ye, C., Zhang, C.L., Catoire, V., Liu, P.F., Gu, R.R., Zhang, J.W., Ma, Z.B., Zhao, X.X., Zhang,
1118   W.Q., Ren, Y.G., Krysztofiak, G., Tong, S.R., Xue, L.K., An, J.L., Ge, M.F., Mellouki, A., Mu, Y.J.,
1119   2021. Evidence for Strong HONO Emission from Fertilized Agricultural Fields and its Remarkable
1120   Impact on Regional O_3 Pollution in the Summer North China Plain. ACS Earth Space Chem. 5, 340-
1121   347.

1122 Yang, K., Kong, L., Tong, S., Shen, J., Chen, L., Jin, S., Wang, C., Sha, F., Wang, L., 2021a. Double
1123   High-Level Ozone and $PM_{2.5}$ Co-Pollution Episodes in Shanghai, China: Pollution Characteristics
1124   and Significant Role of Daytime HONO. Atmosphere 12, 557.

1125 Yang, W., Han, C., Yang, H., Xue, X., 2018. Significant HONO formation by the photolysis of nitrates
1126   in the presence of humic acids. Environ Pollut 243, 679-686.

1127 Yang, W., Han, C., Zhang, T., Tang, N., Yang, H., Xue, X., 2021b. Heterogeneous photochemical uptake
1128   of NO_2 on the soil surface as an important ground-level HONO source. Environ. Pollut. 271, 116289.

1129 Ye, C., Gao, H., Zhang, N., Zhou, X., 2016. Photolysis of Nitric Acid and Nitrate on Natural and Artificial
1130   Surfaces. Environmental Science & Technology 50, 3530-3536.

1131 Ye, C., Zhang, N., Gao, H., Zhou, X., 2017. Photolysis of Particulate Nitrate as a Source of HONO and
1132 NO_x. Environmental Science & Technology 51, 6849-6856.

1133 Zhang, H.L., Li, J.Y., Ying, Q., Yu, J.Z., Wu, D., Cheng, Y., He, K.B., Jiang, J.K., 2012. Source
1134   apportionment of $PM_{2.5}$ nitrate and sulfate in China using a source-oriented chemical transport
1135   model. Atmospheric Environment 62, 228-242.

1136 Zhang, J., An, J., Qu, Y., Liu, X., Chen, Y., 2019a. Impacts of potential HONO sources on the
1137   concentrations of oxidants and secondary organic aerosols in the Beijing-Tianjin-Hebei region of
1138   China. The Science of the total environment 647, 836-852.

1139 Zhang, J., Chen, J., Xue, C., Chen, H., Zhang, Q., Liu, X., Mu, Y., Guo, Y., Wang, D., Chen, Y., Li, J.,
1140   Qu, Y., An, J., 2019b. Impacts of six potential HONO sources on HOx budgets and SOA formation
1141   during a wintertime heavy haze period in the North China Plain. The Science of the total
1142   environment 681, 110-123.

1143 Zhang, J., Guo, Y., Qu, Y., Chen, Y., Yu, R., Xue, C., Yang, R., Zhang, Q., Liu, X., Mu, Y., Wang, J., Ye,
1144   C., Zhao, H., Sun, Q., Wang, Z., An, J., 2020a. Effect of potential HONO sources on peroxyacetyl
1145   nitrate (PAN) formation in eastern China in winter. Journal of Environmental Sciences 94, 81-87.

Zhang, J., Ran, H., Guo, Y., Xue, C., Liu, X., Qu, Y., Sun, Y., Zhang, Q., Mu, Y., Chen, Y., Wang, J., An, J., 2022. High crop yield losses induced by potential HONO sources — A modelling study in the North China Plain. Science of The Total Environment 803, 149929.

Zhang, L., Wang, T., Zhang, Q., Zheng, J.Y., Xu, Z., Lv, M.Y., 2016. Potential sources of nitrous acid (HONO) and their impacts on ozone: A WRF-Chem study in a polluted subtropical region. J Geophys Res-Atmos 121, 3645-3662.

Zhang, N., Zhou, X.L., Shepson, P.B., Gao, H.L., Alaghmand, M., Stirm, B., 2009. Aircraft measurement of HONO vertical profiles over a forested region. Geophysical Research Letters 36. doi:10.1029/2009GL038999.

Zhang, Q., Geng, G., 2019. Impact of clean air action on $PM_{2.5}$ pollution in China. Science China Earth Sciences 62, 1845-1846.

Zhang, S., Sarwar, G., Xing, J., Chu, B., Xue, C., Sarav, A., Ding, D., Zheng, H., Mu, Y., Duan, F., Ma, T., He, H., 2021. Improving the representation of HONO chemistry in CMAQ and examining its impact on haze over China. Atmospheric Chemistry and Physics 21, 15809-15826.

Zhang, W., Tong, S., Ge, M., An, J., Shi, Z., Hou, S., Xia, K., Qu, Y., Zhang, H., Chu, B., Sun, Y., He, H., 2019c. Variations and sources of nitrous acid (HONO) during a severe pollution episode in Beijing in winter 2016. The Science of the total environment 648, 253-262.

Zhang, W.Q., Tong, S.R., Jia, C.H., Wang, L.L., Liu, B.X., Tang, G.Q., Ji, D.S., Hu, B., Liu, Z.R., Li, W.R., Wang, Z., Liu, Y., Wang, Y.S., Ge, M.F., 2020b. Different HONO Sources for Three Layers at the Urban Area of Beijing. Environmental science & technology 54, 12870-12880.

Zheng, H., Song, S., Sarwar, G., Gen, M., Wang, S., Ding, D., Chang, X., Zhang, S., Xing, J., Sun, Y., Ji, D., Chan, C.K., Gao, J., McElroy, M.B., 2020. Contribution of Particulate Nitrate Photolysis to Heterogeneous Sulfate Formation for Winter Haze in China. Environmental Science & Technology Letters 7, 632-638.

Zhou, X., Gao, H., He, Y., Huang, G., Bertman, S.B., Civerolo, K., Schwab, J., 2003. Nitric acid photolysis on surfaces in low-NO_x environments: Significant atmospheric implications. Geophysical Research Letters 30. doi:10.1029/2003GL018620.

Zhu, C., Xiang, B., Zhu, L., Cole, R., 2008. Determination of absorption cross sections of surface-adsorbed HNO_3 in the 290–330 nm region by Brewster angle cavity ring-down spectroscopy. Chemical Physics Letters 458, 373-377.

Zhu, Y.W., Liu, W.Q., Fang, J., Xie, P.H., Dou, K., Qin, M., Si, F.Q., 2011. Monitoring and Analysis of Vertical Profile of Atmospheric HONO, NO_2 in Boundary Layer of Beijing. Spectroscopy and Spectral Analysis 31, 1078-1082.